COMPUTATIONAL MODELLING OF HYDROGEN-INDUCED FAILURE IN METALLIC MATERIALS

A THESIS SUBMITTED TO
THE GRADUATE SCHOOL OF NATURAL AND APPLIED SCIENCES
OF
MIDDLE EAST TECHNICAL UNIVERSITY

BY

BERKEHAN TATLI

IN PARTIAL FULFILLMENT OF THE REQUIREMENTS
FOR
THE DEGREE OF MASTER OF SCIENCE
IN
AEROSPACE ENGINEERING

SEPTEMBER 2024

Approval of the thesis:

COMPUTATIONAL MODELLING OF HYDROGEN-INDUCED FAILURE IN METALLIC MATERIALS

submitted by **BERKEHAN TATLI** in partial fulfillment of the requirements for the degree of **Master of Science in Aerospace Engineering Department, Middle East Technical University** by,

Prof. Dr. Naci Emre Altun
Dean, Graduate School of **Natural and Applied Sciences** _____

Prof. Dr. Serkan Özgen
Head of Department, **Aerospace Engineering** _____

Assoc. Prof. Dr. Tuncay Yalçınkaya
Supervisor, **Aerospace Engineering, METU** _____

Examining Committee Members:

Prof. Dr. Demirkan Çöker
Aerospace Engineering, METU _____

Assoc. Prof. Dr. Tuncay Yalçınkaya
Aerospace Engineering, METU _____

Assoc. Prof. Dr. Ercan Gürses
Aerospace Engineering, METU _____

Assist. Prof. Dr. Görkem Eğemen Güloğlu
Aerospace Engineering, METU _____

Assist. Prof. Dr. Mehmet Okan Görtan
Mechanical Engineering, Hacettepe University _____

Date:05.09.2024

I hereby declare that all information in this document has been obtained and presented in accordance with academic rules and ethical conduct. I also declare that, as required by these rules and conduct, I have fully cited and referenced all material and results that are not original to this work.

Name, Surname: Berkehan Tatlı

Signature :

ABSTRACT

COMPUTATIONAL MODELLING OF HYDROGEN-INDUCED FAILURE IN METALLIC MATERIALS

Tatlı, Berkehan
M.S., Department of Aerospace Engineering
Supervisor: Assoc. Prof. Dr. Tuncay Yalçınkaya

September 2024, 88 pages

The phenomenon of hydrogen-induced failure, which affects a wide range of metals, has attracted significant interest in recent times. This phenomenon arises when hydrogen particles diffuse and relocate within the lattice structure of metallic materials upon exposure to a hydrogen-producing environment. Literature on hydrogen-induced failure has demonstrated that the existence of hydrogen atoms within the lattice structure of metallic materials profoundly affects both the onset and propagation of cracks, resulting in decreased ductility, strength, toughness, and fatigue life [1]. Several theories have been proposed to explain the various mechanisms involved in hydrogen-induced failure, such as hydrogen-enhanced plasticity and hydrogen-enhanced decohesion. These mechanisms connect hydrogen-induced damage to the interactions occurring between hydrogen and imperfections within the material. Therefore, it is crucial to accurately describe the progression of material defects and migration of hydrogen to comprehend hydrogen-induced failure. In this thesis, a potential-based mixed-mode cohesive zone model is coupled with stress-driven hydrogen transport and constitutive frameworks including isotropic Von Mises plasticity, crystal plasticity, and strain gradient crystal plasticity. This framework is used to model

the hydrogen-enhanced decohesion mechanism, focusing on hydrogen-induced intergranular failure as the primary failure mechanism. Initially, 2D Von Mises plasticity simulations are used to validate the proposed novel framework against data from notched specimens, showing a strong correlation with experimental results. Then, crystal plasticity and strain gradient plasticity simulations are conducted on the generated and preprocessed 3D polycrystalline RVEs to examine the size and nonlocal effects in the micromechanical modeling of hydrogen-induced failure.

Keywords: Hydrogen-induced failure, Cohesive zone modeling, Strain gradient crystal plasticity, Size effect, Polycrystalline materials

ÖZ

METALİK MALZEMELERDE HİDROJEN KAYNAKLI KIRILMANIN HESAPLAMALI MODELLENMESİ

Tatlı, Berkehan
Yüksek Lisans, Havacılık ve Uzay Mühendisliği Bölümü
Tez Yöneticisi: Doç. Dr. Tuncay Yalçınkaya

Eylül 2024 , 88 sayfa

Hidrojen kaynaklı malzeme hasarı fenomeni, birçok metalik malzemeyi etkileyen ve son zamanlarda önemli bir ilgi gören bir konudur. Bu fenomen, hidrojen atomlarının metalik malzemelerin kafes yapısı içinde difüze olarak yer değiştirmesi sonucu ortaya çıkar ve bu durum genellikle hidrojen üreten bir ortamla temas halinde gerçekleşir. Hidrojen kaynaklı malzeme hasarı üzerine yapılan çalışmalar, hidrojen atomlarının metalik malzemelerin kafes yapısında bulunmasının, çatlak oluşumu ve yayılımını fazlasıyla etkilediğini ve bunun sonucunda süneklik, dayanım, tokluk ve yorulma ömründe azalmalar meydana geldiğini göstermektedir [1]. Hidrojen kaynaklı malzeme hasarını açıklayan çeşitli teoriler ortaya atılmıştır, bunlardan hidrojen destekli lokalize plastisite ve hidrojen destekli dekohezyon mekanizmaları öne çıkmaktadır. Bu mekanizmalar, hidrojenin malzeme içindeki kusurlar ve dislokasyonlar ile etkileşimlerini tanımlayarak hasarın nasıl meydana geldiğini açıklar. Dolayısıyla, hidrojen kaynaklı hasarı anlayabilmek için malzeme kusurlarının ilerleyişini ve hidrojenin malzeme içindeki taşınımını doğru bir şekilde tanımlamak büyük önem taşımaktadır. Bu tezde, hidrojenin gerilme etkisi ile taşınımı, izotropik Von Mises plastisitesi, kristal plasti-

site ve gerinim gradyanı kristal plastisite gibi malzeme modelleri ile potansiyel tabanlı karışık modlu kohezif alan modeliyle birleştirilmektedir. Bu formülasyon, asıl olarak hidrojen kaynaklı intergranüler hasarın birincil hasar mekanizması olarak incelendiği hidrojen destekli dekohezyon mekanizmasını modellemek amacıyla kullanılmaktadır. İlk olarak, iki boyutlu Von Mises plastisite simülasyonları, çentikli numunelere ait deneysel verilerle karşılaştırılarak önerilen formülasyonun doğruluğu test edilmiştir ve deneylerle yakın sonuçlar elde edilmiştir. Daha sonra, hidrojen kaynaklı hasarın mikromekanik modellemesinde boyut ve yerel olmayan etkileri incelemek amacıyla, oluşturulan üç boyutlu çok tanecikli temsili hacim elemanları üzerinde kristal plastisite ve gerinim gradyanı kristal plastisite simülasyonları gerçekleştirilmiştir.

Anahtar Kelimeler: Hidrojen kaynaklı hasar, Kohezif alan modellemesi, Gerinim gradyanı kristal plastisite, Boyut etkisi, Çok tanecikli malzemeler

To my family and Mümtaz

ACKNOWLEDGMENTS

I am deeply grateful to my supervisor, Assoc. Prof. Dr. Tuncay Yalçınkaya, whose guidance, patience, and belief in my potential have been invaluable throughout this journey. Beyond his academic advice, he provided constant encouragement and support, both professionally and personally. His openness and friendship made this process much more rewarding. I'm truly thankful for the trust we have built and feel fortunate to have had his mentorship.

I would also like to express my heartfelt gratitude to Sena Yolcu. She stood by my side during tough times, and her inspiring smile lifted me up whenever I felt down. The peace I feel when I'm with her and everything she has brought into my life is something I am deeply grateful for. Her love and constant support have been my greatest sources of strength. I couldn't have written this thesis without the inspiration she has given me.

I would like to acknowledge Can Erdoğan, Hande Vural, and Orhun Bulut for their help and input on my thesis. I'm especially thankful to Enes Günay, whose assistance was crucial in completing this work.

A big thank you goes to my best friends, Murad İlhan, Yusuf Pekmezci, Erkin Ünsal, and Batuhan Odabaşı, whose support and encouragement have meant the world to me during this journey. Your companionship made the challenges easier to face, and I am thankful for the countless moments of laughter and motivation we've shared.

Special thanks are due to my family: my mother, Burcu Çınar, my father, Bülent Tatlı, my brother, Arda Çınar, and my grandmother, Feruzan Küçtekin. Your love and support have been my greatest strength throughout this process. You have made this journey more meaningful, and I am deeply grateful for always having you by my side.

Finally, thanks to TÜBİTAK for supporting me through the BİDEB 2210-A program.

TABLE OF CONTENTS

LIST OF TABLES

TABLES

LIST OF FIGURES

FIGURES

CHAPTER 1

INTRODUCTION

Hydrogen-induced failure, often termed hydrogen embrittlement, is a complex phenomenon that affects a wide spectrum of metals and has attracted considerable attention in recent years. This phenomenon occurs when hydrogen particles diffuse and relocate within the lattice structure of metallic materials upon interaction with a hydrogen-producing environment. Experimental studies on hydrogen-induced failure have revealed that the presence of hydrogen atoms within the lattice structure significantly effects both the initiation and propagation of cracks, leading to reduced ductility [1], strength [2, 3], fracture toughness [4, 5, 6], and fatigue life [7, 8, 9].

High-strength materials are particularly vulnerable to hydrogen embrittlement when exposed to hydrogen-rich environments. Materials prone to hydrogen embrittlement include high-strength steels, high manganese steel, aluminum alloys, titanium, magnesium, and magnesium alloys, among others [10, 11, 12]. These high-strength steels are widely used in various industries, including aerospace, nuclear power, hydrogen storage/transportation, and automotive applications. Several factors influence a material's susceptibility to hydrogen embrittlement. These include the material's microstructure, strength, and residual stress, as well as the concentration of hydrogen and the presence of hydrogen traps. The applied strain rate, surface condition, and heat treatment history of the material are also significant factors. Environmental conditions, such as pressure, temperature, exposure time, and the presence of reactive solutions (like acidic environments), along with specific precipitates and metallic coatings, further influence a material's vulnerability to hydrogen embrittlement. The primary characteristic of hydrogen embrittlement is its sensitivity to strain rate and its tendency to cause delayed failure. Hydrogen embrittlement is more pronounced at

lower strain rates [13].

Several theories have been proposed to explain the various mechanisms involved in hydrogen-induced failure, but there is still no consensus on a unified physical mechanism that encompasses the general degradation process [14]. The debate persists in the literature, even after nearly one hundred and fifty years since the effects of hydrogen on metals were first recognized [15]. The primary mechanisms responsible for hydrogen embrittlement, as widely discussed in the literature, include hydrogen-enhanced decohesion (HEDE), hydrogen-enhanced localized plasticity (HELP), hydrogen-induced phase transformation (HIPT), nanovoid coalescence (NVC), with some studies suggesting that a combination of these mechanisms leads to the degradation of mechanical properties and embrittlement of the material [16].
The HEDE mechanism is first identified by [17]. This mechanism is mainly based on the degradation of cohesive strength due to the introduction of hydrogen atoms inside the metal. It has been observed that hydrogen atoms weaken the metallic inter-atomic bonds of the host material by interacting with the outermost electrons, causing separation to occur under lower stress levels than usual. The HEDE mechanism is supported by both theoretical calculations and the observation of intergranular fracture. In this type of fracture, hydrogen, similar to impurity elements like sulfur, phosphorus, and bismuth, segregates at grain boundaries and weakens the cohesive interactions between metal atoms. This reduction in atomic cohesion leads to intergranular fracture [18]. The potential accumulation regions for hydrogen within the material have been identified as areas of maximum hydrostatic stress, dislocation shielding zones near the crack tip, and grain or phase boundaries at the crack tip. [19] reports that the hydrogen concentration near the crack tip is primarily influenced by three factors: lattice concentration, concentration driven by hydrostatic stress, and concentration induced by plastic strain. As noted by [20], in high-strength steels, the crack tip hydrogen concentration is primarily driven by hydrostatic stress, even at low levels of plastic strain.
The HELP mechanism is introduced firstly by [21]. In this model, the hydrogen accumulated near the crack tip decreases the resistance for dislocation motion so that mobility of dislocation increases and dislocations behave as carriers of plastic deformation in a metal lattice [22]. In contrast to the HEDE mechanism, the HELP mech-

anism significantly involves the host metal's plastic response in hydrogen-assisted fracture. [23, 14] demonstrated through in-situ transmission electron microscope (TEM) experiments that the presence of hydrogen within a metal increases dislocation mobility. Hydrogen not only initiates the movement of stationary dislocations but also accelerates the rate of dislocation nucleation. The experiments also revealed that once hydrogen is removed from the system, the direction of dislocation motion reverses. While the HELP mechanism has been widely used to explain hydrogen embrittlement, certain phenomena remain unexplained by this theory. For example, macroscopic tensile tests on IN718 alloys show that hydrogen induces the Portevin-Le Chatelier effect by suppressing dislocation motion, which contradicts the predictions of the HELP mechanism [24]. Another conflicting finding is reported in [25], where in situ microscopic tensile tests confirm that dislocations in pure aluminum are also dragged by hydrogen. Once the hydrogen supply is removed, the previously pinned dislocations recover and resume movement.

The mechanism of HESIV is first introduced in the literature by [26]. This mechanism suggests that hydrogen accelerates the formation of strain-induced vacancies and stabilizes vacancy clusters, as supported by positron annihilation lifetime spectroscopy [27] and molecular dynamics simulations [28]. As a result, these vacancy clusters promote void initiation and growth, leading to premature failure.

In the HIPT theory, certain metals like Zr, Nb, V, and Ta readily combine with hydrogen to form brittle hydrides due to their high bond energies. This mechanism consists of four main stages [29]: (1) hydrogen diffuses and accumulates at the crack tip; (2) hydrides form and grow; (3) a crack initiates along a specific cleavage plane within the hydrides; and (4) the crack is arrested at the matrix/hydride interfaces. Repeated cycles of these steps eventually lead to crack propagation. In some cases, hydrogen atoms from the decomposed hydrides diffuse back toward areas of stress concentration, leading to the formation of new brittle hydrides and further intensifying brittle cleavage fracture [30].

The NVC mechanism, first introduced by [2], integrates the combined effects of the HEDE, HELP, and HESIV mechanisms. It is important to note that these mechanisms are primarily based on postmortem observations of samples, which cannot directly confirm the reduction in cohesive strength due to hydrogen in the HEDE mechanism or the enhancement of dislocation motion by hydrogen in the HELP mechanism.

In recent years, the activation of HEDE and HELP mechanisms has been identified through observations of fracture surfaces and microstructural evolution. The HEDE mechanism is active during intergranular fracture, while the HELP mechanism is triggered when hydrogen-assisted cracking initiates at the intersections of slip bands. [31] and [18] observed a combination of brittle hydrogen-assisted fracture surface features along with microstructural evolution beneath the intergranular fracture, indicating a synergistic effect between the HEDE and HELP mechanisms. This combined mechanism has also been supported by a statistical, physically-based, and micromechanical model of hydrogen-induced intergranular fracture in steels [16, 32]. Figure 1.1 summarizes the main physical mechanisms of the hydrogen-induced failure.

Several modelling techniques have been widely used in the literature to capture the effect of hydrogen-induced failure based on the aforementioned physical mechanisms. These modelling techniques range from molecular dynamics simulations at the microscale to hydrogen-induced plasticity laws at the macroscale.
[35] employed direct molecular dynamics simulations to investigate the ductile-to-brittle fracture transition caused by the accumulation of hydrogen atoms at the crack tip, which limits dislocation emission. The authors suggest that hydrogen accumulation near the crack tip, driven by the stress field, suppresses dislocation mobility, thereby reducing the material's capacity for ductile fracture. In the study of [36] conducted molecular dynamics simulations on polycrystalline α-iron at various hydrogen concentrations and grain sizes. The study found that increasing hydrogen concentration led to a more significant reduction in fracture resistance in fine-grained polycrystals compared to coarse-grained polycrystals. [37] conducted cohesive zone simulations, coupled with molecular dynamics at the microscale, to investigate the effect of hydrogen on intergranular decohesion. Their results demonstrated that hydrogen coverage at grain boundaries significantly lowers the critical stress in the traction-separation law.
Phase field fracture modelling is also a widely used approach in the literature, as it effectively captures complex crack paths and can simulate transgranular fractures observed at the microscale [38]. The theory is grounded in the concept of energy minimization, making it particularly suited for such applications. [39] combines hydrogen diffusion with mechanical deformation and models hydrogen-induced fracture

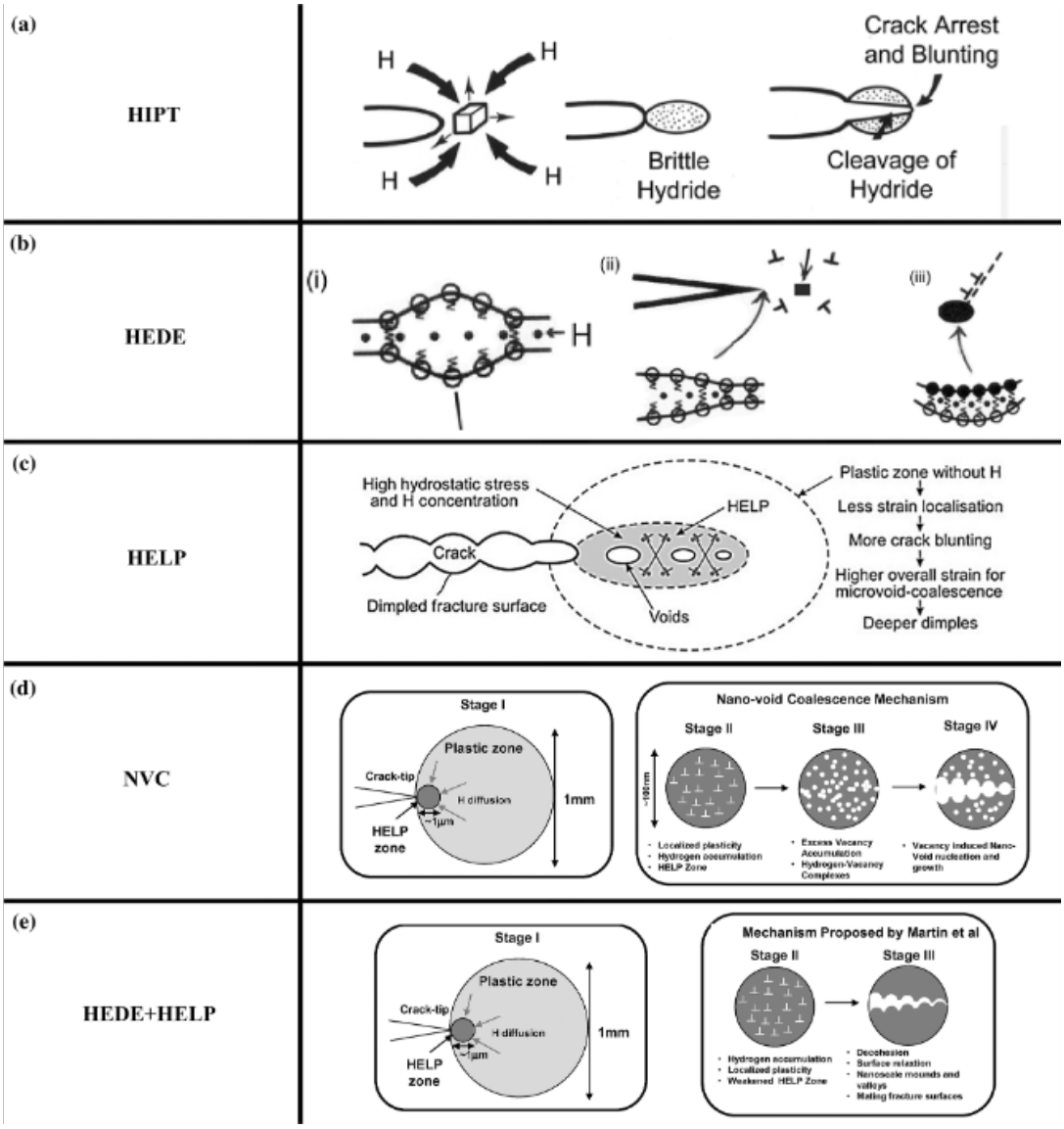

Figure 1.1: Summary of the primary mechanisms for hydrogen-induced failure, as suggested in the literature [2, 33, 34]

by reducing the fracture energy based on empirical first-principle calculations. The study demonstrates that this coupled framework can accurately predict unstable crack growth, the sensitivity of failure stress in notched specimens to hydrogen, and the complex crack paths observed in macroscopic specimens due to corrosion pits. The study by [40] models the effects of HELP, and HEDE by reducing the yield stress and critical energy release rate of the material, focusing on macroscopic compact tension and double-notched tension specimens. The findings indicate that hydrogen tends to accumulate at crack or notch tips due to elevated hydrostatic stress and the increased

number of traps generated by the high plasticity observed in these regions.

The phase field fracture framework has also been applied to the model the failure in hydrogen transport pipelines. [41] examined the effect of hydrogen on dented pipelines using the phase field fracture method, concluding that increasing hydrogen concentration significantly reduces the maximum dent depth. Additionally, [42] implemented a second-order phase field fracture framework coupled with an elasto-plastic phenomenological plasticity model for deformation and a hydrogen diffusion model driven by the gradient of hydrostatic stress. This study investigated the failure of X65 pipelines, demonstrating premature crack tearing, an accelerated crack propagation rate, and a reduction in the load-bearing capacity of the material.

Multiple studies in the literature have utilized the phase field method to predict fatigue crack growth [43, 44, 45]. [46] employed a coupled framework combining deformation, diffusion, and damage modelling to predict fatigue crack growth and nucleation under various loading conditions and geometries. Virtual experiments demonstrated that the phase field method aligns well with experimental data for both notched and smooth samples. [47] combines a phase field fatigue fracture formulation with stress-assisted hydrogen diffusion, incorporating material toughness degradation to account for the effects of both cyclic loading and hydrogen concentration. [48] investigates the corrosion fatigue of carbon steels using a framework that effectively couples the displacement field for mechanical deformation, the electrochemical field for corrosion, and the phase field for fracture. Accumulated fatigue damage is accounted for by degrading the free energy density at the interface, considering both elastic and plastic strain energies. The framework is validated by comparing pure fatigue and corrosion-fatigue damage in compact tension specimens with experimental results. The study highlights the increased crack growth rate due to the coupling effects of corrosion-fatigue and underscores the critical role of plasticity.

Another widely utilized computational framework in the literature for simulating hydrogen-induced failure is cohesive zone modelling. This framework primarily involves two constitutive models: the first is the classical constitutive law, which defines the stress based on the strain in the bulk regions of the material, and the second is the traction-separation law, or cohesive law, which defines the traction (the force between adjacent crack faces) as a function of the separation between cohesive

zone elements inserted along the crack propagation surfaces. This framework is applied in both microscale studies, such as simulating representative volume elements (RVEs) to investigate the influence of microstructural features on macroscopic behavior [49, 50, 51, 52], and in macroscale studies, such as estimating fatigue crack growth in gaseous hydrogen environments [53], reproducing fracture mechanics tests to obtain fracture resistance curves, including crack tip opening displacement (R-curves) [54, 55], or load versus crack mouth opening displacement (CMOD) curves [56]. [57] models the combined effect of two physical mechanisms, HELP and HEDE, in dissimilar welds by employing cohesive zone elements. The traction-separation law for these elements is made a function of both the hydrogen content and the plastic deformation of the surrounding material, particularly for carbide-matrix decohesion mechanisms. Additionally, a constitutive model that also depends on hydrogen content is used to further capture the material behavior. Experimental data on notched specimens from [58] were simulated using a cohesive zone framework where the cohesive strength was degraded based on hydrogen content. The study emphasizes that the hydrogen degradation law should not only depend on hydrogen concentration but must also account for geometric factors, specifically stress triaxiality, which reflects the mechanical influence of geometry and loading conditions. This suggests that the degradation law should not be viewed as an intrinsic material property alone but should also capture the material's stress state. [59] investigates the ductile tearing behavior of high-strength AISI 4130 steel through two-dimensional compact tension specimen simulations. Their framework incorporates the HELP mechanism by reducing the flow stress with increasing hydrogen concentration and the HEDE mechanism by introducing zero-thickness cohesive zone elements, where the traction-separation law is hydrogen concentration-dependent. After thoroughly calibrating the interface properties, the simulation results demonstrated a high level of accuracy in effectively modelling the ductile failure of macroscopic specimens. [60] examines the effects of grain size and misorientation on hydrogen embrittlement in nickel using a cohesive zone model informed by hydrogen content. The study concludes that grain misorientation significantly weakens the material. For a more in-depth analysis of grain misorientation effects, refer to [61]. Additionally, it confirms the inverse relationship between material strength and grain size, consistent with the Hall-Petch effect. The findings also show that larger grains delay hydrogen diffusion to crack initiation and

propagation sites due to the longer diffusion paths. Consequently, the reduction in material strength due to hydrogen embrittlement is less pronounced in larger grain microstructures, as hydrogen has less time to concentrate at the crack tip. An interesting study by [62] combines phase field and cohesive zone modelling approaches to simultaneously predict transgranular and intergranular fractures. The research examines two-dimensional polycrystalline microstructures to capture the transition from ductile (transgranular) failure, modeled using a phase field fracture approach, to brittle (intergranular) failure, described by the cohesive zone framework. This transition is a well-known phenomenon that occurs under the influence of hydrogen.
Several studies in the literature have employed a phase-field regularized cohesive zone model to simulate hydrogen-induced failure. [63] addresses the limitations of the cohesive zone model, which primarily predicts intergranular failure, and the phase field fracture model, which lacks the ability to capture cohesive fractures. The authors introduce a novel approach grounded in the unified phase field theory [64], which can model both brittle and cohesive fractures while being independent of length scale, as demonstrated in a comparative study by [65]. Simply put, the framework integrates the HEDE mechanism to reduce the critical energy release rate in the phase field fracture model, allowing for the prediction of damage initiation and propagation under hydrogen influence. This is achieved through the coupled response of the mechanical and diffusion problems [66]. [67] extends the given framework to account for fatigue-induced crack initiation and propagation. The study evaluates the extended model's performance across various fatigue behaviors, including hysteresis loops, fatigue–creep interaction curves, and Paris law. Both two-dimensional and three-dimensional boundary value problem simulations are conducted under different loading conditions, with the results showing good agreement with experimental data for concrete-like materials.

In the existing literature, various material laws have been proposed for constitutive modelling of materials susceptible to hydrogen-induced failure. While many studies utilize isotropic Von Mises plasticity models [68, 69, 70], others advocate for more advanced approaches, including strain gradient plasticity [71, 72, 73, 74], crystal plasticity [75, 76, 77, 78, 79, 80], strain gradient crystal plasticity [81], hydrogen-informed continuum plasticity or damage models [82, 83, 84, 85, 86] and microme-

chanical models [87, 88, 89, 90, 91].

[71] presents a hydrogen transport model that incorporates both first-order hydrogen flux, driven by plastic strain, and second-order hydrogen flux, driven by gradients of plastic strain. The study demonstrates that the first-order hydrogen flux has negligible importance, even in nickel, a material with low hydrogen diffusivity. Instead, the second-order hydrogen flux, driven by plastic strain gradients, leads to hydrogen accumulation near grain boundaries during deformation. This accumulation is identified as a key factor in driving intergranular cracking, as observed in microstructural experiments. The paper argues that the intrinsic plastic heterogeneity resulting from grain misorientation induces substantial plastic strain gradients at grain boundaries. Therefore, these gradients must be incorporated into hydrogen-induced failure simulations of polycrystalline structures to accurately capture intergranular cracking. [72, 74] also emphasizes the critical role of strain gradients in simulating fracture in hydrogen-rich environments. The study demonstrates that incorporating strain gradient plasticity as a constitutive law for hydrogen-embrittlement-prone materials significantly increases the geometrically necessary dislocation (GND) density at the crack tip, thereby raising the flow stress. As the stress around the crack tip rises due to strain gradient effects, so does the hydrostatic stress, leading to higher hydrogen concentrations and more trapped hydrogen near the crack tip, which exacerbates the damage accumulation. It is clearly demonstrated that GNDs, which are absent in conventional plasticity formulations, play a vital role in significantly raising both stress levels and hydrogen lattice concentration in the region directly ahead of the crack tip. The findings show good agreement with experimental data for ultra-high-strength steels such as Monel® K-500, AerMet™100, and Ferrium™M54.

To examine the influence of microstructural features, such as texture and grain morphology, on the macroscopic response, several studies integrate local or nonlocal crystal plasticity formulations (like strain gradient crystal plasticity) into their coupled mechanical deformation–diffusion frameworks. [81] investigates the impact of microstructure, stress concentration factors, and loading conditions on zirconium polycrystals by employing a non-local crystal plasticity formulation coupled with hydrogen transport equations. The study examines hydrogen accumulation in the lattice to assess the independent effects of texture and microstructure. It concludes that hydrogen tends to accumulate near grain boundaries, particularly at triple-junction points,

and in regions with high strain levels due to localized deformation, where dislocations concentrate. These factors can significantly influence the material's behavior under hydrogen exposure. [80] extends their physically-based rate-dependent crystal plasticity formulation to incorporate hydrogen concentration into the constitutive relations. The study focuses on the initial and post-yield strain hardening behavior of single-crystal stainless steel 316L, aiming to link mesoscale microstructural effects with experimental findings. [92] presents a framework that couples crystal plasticity with hydrogen diffusion to investigate hydrogen transport and storage in generic two-dimensional polycrystalline microstructures, highlighting micromechanical modelling as a powerful tool for understanding hydrogen's effect at the microscale. The study primarily explores the impact of stress states on hydrogen diffusion and the accumulation of hydrogen around dislocations generated in regions of localized plastic strain. In [76], a dislocation-density-based crystal plasticity formulation is implemented to study the HELP failure mechanism. Crystal plasticity finite element simulations are conducted for polycrystalline Pd-H and Ni-H alloys to explore hydrogen's influence on plasticity. The study highlights several hydrogen-dependent behaviors, including an increase in flow stress, hydrogen-enhanced dislocation multiplication, increased heterogeneity in plastic deformation due to the hydrogen-induced delay in the exhaustion of plastic flow in softer grains, and hydrogen-enhanced strain localization.

Building upon the discussed physical failure mechanisms, fracture modelling techniques, and constitutive laws for simulating materials under hydrogen influence, this thesis focuses on investigating the hydrogen-enhanced decohesion (HEDE) mechanism. This is achieved using a PPR potential-based mixed-mode cohesive zone model, coupled with mechanical deformation and stress-driven hydrogen diffusion. Isotropic Von Mises plasticity, Crystal Plasticity, and Strain Gradient Crystal Plasticity constitutive models are employed for both macroscale and microscale analyses. The coupled framework is implemented in both two-dimensional and three-dimensional simulations. While the framework is validated through two-dimensional macroscopic notched specimen simulations, the primary results are derived from generic three-dimensional polycrystalline microstructures. An extensive preprocessing, detailed in Chapter 3, is carried out using several in-house scripts on the gener-

ated input files for polycrystalline structures. Initially, grain boundary interfaces are identified for the insertion of cohesive zone elements. Subsequently, contact surfaces are defined to allow hydrogen transport between adjacent grains, bypassing the cohesive zone elements at each interface. Simulated polycrystalline microstructures are generated through a Voronoi tessellation algorithm for various grain size and number of grains. The influence of microstructure on the homogenized macroscopic response of the material is analyzed by comparing results from crystal plasticity finite element simulations. This comparison involves both macroscopic stress-strain curves and microscopic observations, such as hydrogen accumulation regions and localized stress and strain concentrations. Strain gradient crystal plasticity simulations are subsequently conducted to examine the nonlocal effects on the failure of polycrystalline structures under the influence of hydrogen. As noted in the literature, the role of GNDs in stress concentration regions, particularly near the crack tip, is crucial and should not be overlooked. By integrating the strain gradient effect into the crystal plasticity formulations and comparing hydrogen accumulation, stress concentration, and intergranular crack propagation patterns in polycrystalline RVEs, several qualitative conclusions are drawn and presented.

The thesis is organized as follows: Chapter 2 provides details of the constitutive models used in the simulations, including the formulation of the Park-Paulino-Roesler cohesive zone model, the hydrogen transport model, and the numerical coupling and implementation of the framework. Chapter 3 covers the numerical modelling, beginning with the generation of polycrystalline RVEs, followed by an explanation of the preprocessing steps applied to the input files, the boundary conditions used, and the volumetric homogenization method. This chapter also presents the numerical results, including both two-dimensional macroscopic simulations used to verify the framework, and three-dimensional polycrystalline RVE simulations to examine microstructural effects. Finally, Chapter 4 provides a summary of the findings and conclusions drawn from the results, along with potential areas for future work.

CHAPTER 2

MICROMECHANICAL MODELLING OF HYDROGEN-INDUCED FAILURE

This chapter outlines the constitutive laws employed in the numerical findings presented in Chapter 3, along with the formulation of the potential-based mixed-mode cohesive zone model used to predict intergranular failure. These constitutive models play a critical role in capturing the material behavior under hydrogen-induced failure conditions, ensuring that the complex interactions between hydrogen transport and mechanical deformation are accurately represented. It also details the hydrogen transport equations and their implementation through the established analogy between heat transfer and stress-assisted impurity diffusion equations. Additionally, the chapter explains the calculation scheme for the gradient of hydrostatic stress, a crucial field variable for determining hydrogen flux within the framework. The hydrogen-related degradation laws affecting the cohesive zone parameters through the reduction in cohesive energy or cohesive strength are also introduced. The chapter concludes with a discussion on the implementation of the coupled framework in the commercial finite element solver software ABAQUS, using the user-defined subroutines UMAT, UEL, and UMATHT, followed by an overview of the staggered solution scheme employed.

2.1 Constitutive Models

This section provides a detailed overview of the constitutive models used in this thesis, focusing on the theories of rate-dependent crystal plasticity and lower-order strain gradient crystal plasticity. These are the primary constitutive laws applied throughout the numerical examples discussed in Chapter 3.

2.1.1 Rate Dependent Phenomenological Crystal Plasticity

In the crystal plasticity framework, the macroscopic deformation is governed by two fundamental mechanisms: elastic lattice distortion and crystallographic slip induced by the motion of dislocations on active slip systems (see [93, 94]). The finite strain formulation used in the crystal plasticity model implemented in this study incorporates a multiplicative decomposition of the deformation gradient into elastic and plastic components [95, 96], as illustrated in Figure 2.1

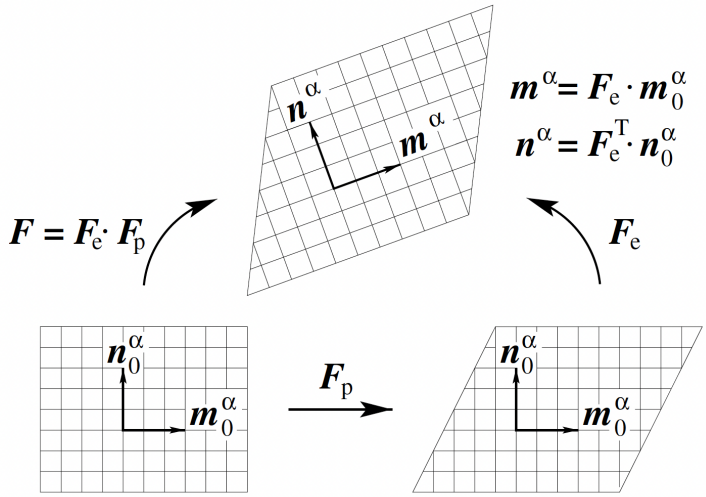

Figure 2.1: Multiplicative decomposition of the deformation gradient [96]

$$\mathbf{F} = \mathbf{F}_e \cdot \mathbf{F}_p \tag{2.1}$$

where $\mathbf{F}_p$ relates plastic deformation due to shearing and $\mathbf{F}_e$ gives elastic stretching and lattice rotation. The velocity gradient tensor is used to calculate the rate of plastic deformation on each slip system, which is related to the shear stress acting on the slip system.

$$\mathbf{L} = \dot{\mathbf{F}} \cdot \mathbf{F}^{-1} = \mathbf{L}_e + \mathbf{L}_p \tag{2.2}$$

$$\mathbf{L}_p = \dot{\mathbf{F}}_p \cdot \mathbf{F}_p^{-1} = \sum_\alpha \dot{\gamma}^\alpha \mathbf{m}^\alpha \otimes \mathbf{n}^\alpha \tag{2.3}$$

where $\mathbf{m}^{\alpha}$ is the slip direction and $\mathbf{n}^{\alpha}$ is the slip normal in the reference state. These vectors deform with the $\mathbf{F}_e$ as:

$$\mathbf{m}^{\alpha} = \mathbf{F}_e \cdot \mathbf{m}_0^{(\alpha)} \tag{2.4}$$

$$\mathbf{n}^{\alpha} = \mathbf{F}_e^{\mathrm{T}} \cdot \mathbf{n}_0^{(\alpha)} \tag{2.5}$$

The rate of plastic shear can be related to the current resolved shear stress, $\tau^{\hat{\alpha}}$, as

$$\dot{\gamma}^{\hat{\alpha}} = \dot{\gamma}_0 \left| \frac{\tau^{\hat{\alpha}}}{g^{\hat{\alpha}}} \right|^{\mathcal{N}} sign(\tau^{\hat{\alpha}}) \tag{2.6}$$

where $\tau^{\hat{\alpha}}$ is the resolved shear stress, $\dot{\gamma}_0$ is the reference slip rate. $g^{\hat{\alpha}}$ defines the slip resistance on the slip system $\hat{\alpha}$ that controls the hardening of the single crystal and $\mathcal{N}$ denotes the rate sensitivity parameter. The evolution of slip resistance is governed by,

$$\dot{g}^{\hat{\alpha}} = \sum_{\hat{\beta}} h^{\hat{\alpha}\hat{\beta}} \left| \dot{\gamma}^{\hat{\beta}} \right| \tag{2.7}$$

with $h^{\hat{\alpha}\hat{\alpha}}$ and $h^{\hat{\alpha}\hat{\beta}}$ defining the self-hardening rate and latent hardening matrix respectively. The evolution of these is described by the following basic forms,

$$h^{\hat{\alpha}\hat{\alpha}} = h_0 sech^2 \left| \frac{h_0 \gamma}{g_s - g_0} \right| \quad , \quad h^{\hat{\alpha}\hat{\beta}} = q^{\hat{\alpha}\hat{\beta}} h^{\hat{\alpha}\hat{\alpha}} \quad (\hat{\alpha} \neq \hat{\beta}) \tag{2.8}$$

where h_0 is the initial hardening modulus, g_0 is the initial slip resistance and g_s is the saturation slip resistance. This model considers plastic deformation to occur entirely from crystallographic dislocation slip and does not incorporate other mechanisms such as diffusion, grain boundary sliding, or nonlocal effects. Throughout all numerical simulations involving crystal plasticity framework, the reference slip rate $\dot{\gamma}_0$ is taken to be 0.0001 s^{-1}, while rate sensitivity exponent $\mathcal{N}$ is defined as 25 and the ratio of latent to self-hardening is assumed to be 1.

2.1.2 Lower Order Strain Gradient Crystal Plasticity Theory

This thesis employs the mechanism-based strain gradient crystal plasticity theory proposed by [97] to capture size effects and incorporate nonlocal crystal plasticity behavior into the numerical framework. In this formulation, geometrically necessary dislocations (GNDs) are integrated using the Taylor relation [98].

The slip law from the local crystal plasticity formulation, see 2.6, is modified to include the hardening effect due to the GNDs, as follows:

$$\dot{\gamma}^{\hat{\alpha}} = \dot{\gamma}_0 \left| \frac{\tau^{\hat{\alpha}}}{g^{\hat{\alpha}}_{TOT}} \right|^{\mathcal{N}} sign(\tau^{\hat{\alpha}}) \tag{2.9}$$

where $g^{\hat{\alpha}}_{TOT}$ is the effective slip resistance that is defined by the addition of the hardening due to the GNDs on top of the statistically stored dislocations (SSDs), as follows:

$$g^{\hat{\alpha}}_{TOT} = \sqrt{{g^{\hat{\alpha}}_{SSD}}^2 + {g^{\hat{\alpha}}_{GND}}^2} \tag{2.10}$$

where $g^{\hat{\alpha}}_{SSD}$ is the slip resistance through the SSDs and $g^{\hat{\alpha}}_{GND}$ is the slip resistance through the GNDs on a slip system $\hat{\alpha}$. Evolution of the slip resistance due to the SSDs is the same as given in 2.7:

$$\dot{g}^{\hat{\alpha}}_{SSD} = \sum_{\hat{\beta}} h^{\hat{\alpha}\hat{\beta}} \left| \dot{\gamma}^{\hat{\beta}} \right| \tag{2.11}$$

Slip resistance due to the GNDs is defined as:

$$g^{\hat{\alpha}}_{GND} = g_0 \sqrt{l \eta^{\hat{\alpha}}_{GND}} \tag{2.12}$$

where g_0 is the initial slip resistance, $\eta^{\hat{\alpha}}_{GND}$ is the GND density on a slip system $\hat{\alpha}$, l is the intrinsic length scale parameter whose definition is given as:

$$l = \frac{{\alpha_T}^2 \mu^2 b}{g_0^2} \tag{2.13}$$

Here, α_T, as described in [99], is a geometrical factor dependent on the type and arrangement of interacting dislocations, typically ranging between 0.2 and 0.5. μ denotes the shear modulus of the material, b represents the length of the Burgers vector, and g_0 is the initial slip resistance of the crystal. The length scale parameter primarily controls the hardening effect due to the GNDs and should be comparable to the characteristic length of the model. As the length scale parameter decreases, the observed size effect diminishes, and when the length scale parameter approaches zero, the model behaves purely as a local rate-dependent phenomenological crystal plasticity formulation, as described in Subsection 2.1.1. [97] introduced a formulation for calculating the effective density of GNDs within his mechanism-based strain gradient framework, as follows:

$$\eta^{\hat{\alpha}}_{GND} = \left| \mathbf{n}^{\hat{\alpha}} \times \sum_{\hat{\beta}} (\mathbf{m}^{\hat{\alpha}} \cdot \mathbf{m}^{\hat{\beta}}) \nabla \gamma^{\hat{\alpha}} \times \mathbf{n}^{\hat{\alpha}} \right| \tag{2.14}$$

Incorporating the density of GNDs into the model using an intrinsic length scale parameter causes the material behavior to depend on the size and scale of deformations. This approach is employed to model the size-dependent material response in Chapter 3. For more detail on the numerical implementation of the model see [100], and application of the model see [101, 102, 103].

2.2 Park-Paulino-Roesler (PPR) Cohesive Zone Model

The Park-Paulino-Roesler (PPR) [104], an intrinsic, mixed-mode, potential based cohesive zone model, is employed in this thesis to simulate the initiation and propagation of the cracks. The PPR model is regarded as superior to other cohesive zone modelling (CZM) frameworks for simulating intergranular fractures in 3D RVEs due to the mixed-mode nature of the problem. Due to its energetic consistency and computational tractability, the model is particularly useful for problems involving unknown crack paths and high failure mode-mixity [105, 106]. The PPR model depends on four fundamental independent parameters in the normal and shearing fracture modes: cohesive strength, fracture energy, the shape of the softening curve, and the initial slope of the traction–separation relationship. The potential function that defines the model is given by:

$$\psi(\Delta_n, \Delta_t) = min(\phi_n, \phi_t) + \left[\Gamma_n \left(1 - \frac{\Delta_n}{\delta_n}\right)^{\alpha} \left(\frac{m}{\alpha} + \frac{\Delta_n}{\delta_n}\right)^{m} + \langle \phi_n - \phi_t \rangle\right] \times \left[\Gamma_t \left(1 - \frac{|\Delta_t|}{\delta_t}\right)^{\beta} \left(\frac{n}{\beta} + \frac{|\Delta_t|}{\delta_t}\right)^{n} + \langle \phi_t - \phi_n \rangle\right] \quad (2.15)$$

where $\langle \cdot \rangle$ denotes the Macaulay bracket, defined as follows:

$$\langle x \rangle = \begin{cases} 0 & \text{if } x < 0, \\ x & \text{if } x \geq 0. \end{cases} \quad (2.16)$$

Due to the nature of the potential function, the gradients of the potential function given in Equation 2.15 provide the cohesive traction in both tangential and normal

directions.

$$T_n(\Delta_n, \Delta_t) = \frac{\Gamma_n}{\delta_n}\left[m\left(1-\frac{\Delta_n}{\delta_n}\right)^{\alpha}\left(\frac{m}{\alpha}+\frac{\Delta_n}{\delta_n}\right)^{m-1} - \alpha\left(1-\frac{\Delta_n}{\delta_n}\right)^{\alpha-1}\left(\frac{m}{\alpha}+\frac{\Delta_n}{\delta_n}\right)^{m}\right] \times\left[\Gamma_t\left(1-\frac{|\Delta_t|}{\delta_t}\right)^{\beta}\left(\frac{n}{\beta}+\frac{|\Delta_t|}{\delta_t}\right)^{n} + \langle\phi_t-\phi_n\rangle\right] \quad (2.17)$$

$$T_t(\Delta_n, \Delta_t) = \frac{\Gamma_t}{\delta_t}\left[n\left(1-\frac{|\Delta_t|}{\delta_t}\right)^{\beta}\left(\frac{n}{\beta}+\frac{|\Delta_t|}{\delta_t}\right)^{n-1} - \beta\left(1-\frac{|\Delta_t|}{\delta_t}\right)^{\beta-1}\left(\frac{n}{\beta}+\frac{|\Delta_t|}{\delta_t}\right)^{n}\right] \times\left[\Gamma_n\left(1-\frac{\Delta_n}{\delta_n}\right)^{\alpha}\left(\frac{m}{\alpha}+\frac{\Delta_n}{\delta_n}\right)^{m} + \langle\phi_n-\phi_t\rangle\right]\frac{\Delta_t}{|\Delta_t|} \quad (2.18)$$

Here, m and n are non-dimensional exponents, α and β are shape parameters, δ_n and δ_t are the final crack opening widths in the normal and tangential directions, respectively. ϕ_n and ϕ_t are the fracture energies for the normal and tangential directions, while Δ_n represents the normal separation and Δ_t denotes the effective sliding displacement, calculated from the separations in each tangential direction as:

$$\Delta_t = \sqrt{\Delta_{t1}^2 + \Delta_{t2}^2} \quad (2.19)$$

A visualization of a 3D cohesive element in between two eight-node brick elements (C3D8), with local coordinates, is shown in Figure 2.2:

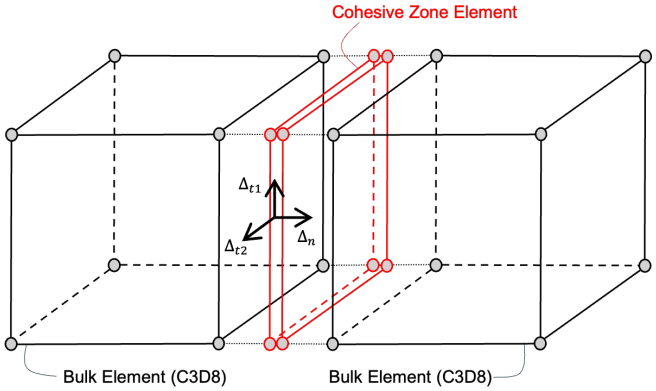

Figure 2.2: Detailed visualization of the 3D cohesive element used in this thesis, including local axes

The model satisfies the following boundary conditions for cohesive fracture:

- For failure to occur in the normal direction, one of the following conditions must be met:

$$T_n(\delta_n, \Delta_t) = 0, \quad T_n(\Delta_n, \overline{\delta}_t) = 0 \tag{2.20}$$

where $\overline{\delta}_t$ represents tangential conjugate final crack opening width.

- For failure to occur in the tangential direction, one of the following conditions must be met:

$$T_t(\overline{\delta}_n, \Delta_t) = 0, \quad T_t(\Delta_n, \delta_t) = 0 \tag{2.21}$$

where $\overline{\delta}_n$ represents normal conjugate final crack opening width.

- The fracture energies ϕ_n and ϕ_t correspond to the areas under the normal and tangential traction-separation curves for $\Delta_t = 0$ and $\Delta_n = 0$, respectively:

$$\phi_n = \int_0^{\delta_n} T_n(\Delta_n, 0)\,\mathrm{d}\Delta_n, \quad \phi_t = \int_0^{\delta_t} T_t(0, \Delta_t)\,\mathrm{d}\Delta_t \tag{2.22}$$

- Critical crack opening widths in the normal and tangential directions (δ_{nc}, δ_{nt}) are defined as the points where the traction-separation curves reach their peaks:

$$\left.\frac{\partial T_n}{\partial \Delta_n}\right|_{\Delta_n=\delta_{nc}} = 0, \quad \left.\frac{\partial T_t}{\partial \Delta_t}\right|_{\Delta_t=\delta_{tc}} = 0 \tag{2.23}$$

- The cohesive traction values at the critical crack opening widths are defined as the cohesive strengths (σ_{max}, τ_{max}):

$$T_n(\delta_{nc}, 0) = \sigma_{\max}, \quad T_t(0, \delta_{tc}) = \tau_{\max}. \tag{2.24}$$

The shape parameters α and β define the softening responses in each direction. Values of these parameters smaller than two result in a concave unloading part of the traction-separation curves, which is more suitable for ductile materials. When their values exceed two, the softening curves become convex, which is more suitable for brittle materials.

λ_n and λ_t are the initial slope indicators that control the initial elastic behavior and cohesive stiffness of the intrinsic cohesive zone model. Smaller values of these indicators lead to higher cohesive stiffness, which in turn reduces artificial compliance. Consequently, λ_n and λ_t are typically chosen to be as small as possible while ensuring numerical stability within the numerical simulations. They are defined as the ratio of

the normal and tangential critical crack opening widths (δ_{nc}, δ_{tc}) to the normal and tangential final crack opening widths (δ_n, δ_t) as follows:

$$\lambda_n = \frac{\delta_{nc}}{\delta_n}, \quad \lambda_t = \frac{\delta_{tc}}{\delta_t} \tag{2.25}$$

Figure 2.3 summarizes the traction-seperation boundary conditions and aforementioned model parameters.

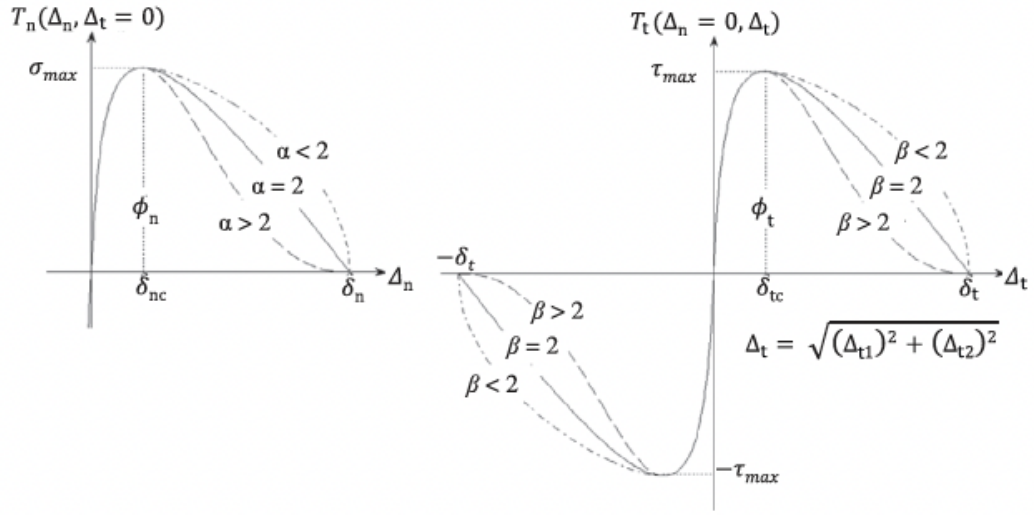

Figure 2.3: Summary of the traction-seperation boundary conditions and PPR CZM parameters

Γ_n and Γ_t are energy constants related to the fracture energies of modes I and II, defined through shape parameters and initial slope indicators as follows:

$$\Gamma_n = \begin{cases} \left(\frac{\alpha}{m}\right)^m, & \phi_n < \phi_t \\ -\phi_n \left(\frac{\alpha}{m}\right)^m, & \phi_n \geq \phi_t \end{cases}$$
$$\Gamma_t = \begin{cases} \left(\frac{\beta}{n}\right)^n, & \phi_t \leq \phi_n \\ -\phi_t \left(\frac{\beta}{n}\right)^n, & \phi_t > \phi_n \end{cases} \tag{2.26}$$

The non-dimensional exponents m and n are the functions of initial slope indicators, (λ_n, λ_t) and shape parameters (α, β) , as follows:

$$m = \frac{\alpha(\alpha-1)\lambda_n^2}{1-\alpha\lambda_n^2}, \quad n = \frac{\beta(\beta-1)\lambda_t^2}{1-\beta\lambda_t^2} \tag{2.27}$$

The normal and tangential final crack opening widths (δ_n, δ_t) can be calculated using

Equation 2.22 and Equation 2.24, yielding the following:

$$\begin{aligned}\delta_n &= \frac{\phi_n}{\sigma_{\max}}\alpha\lambda_n(1-\lambda_n)^{\alpha-1}\left(\frac{\alpha}{m}+1\right)\left(\frac{\alpha}{m}\lambda_n+1\right)^{m-1} \\ \delta_t &= \frac{\phi_t}{\tau_{\max}}\beta\lambda_t(1-\lambda_t)^{\beta-1}\left(\frac{\beta}{n}+1\right)\left(\frac{\beta}{n}\lambda_t+1\right)^{n-1}\end{aligned} \tag{2.28}$$

The model is defined by a total of eight parameters, which are normal and tangential cohesive strengths (σ_{max}, τ_{max}), normal and tangential fracture energies (ϕ_n, ϕ_t), normal and tangential shape parameters (α, β) and normal and tangential initial slope indicators (τ_n, τ_t).

2.3 Hydrogen Transport Model

This section offers a detailed explanation of stress-assisted lattice diffusion of hydrogen, beginning with the derivation of the hydrogen flux. The diffusion process is governed by the chemical potential gradient, driven by the hydrostatic stress gradient and mass balance equations, to determine the time-dependent changes in hydrogen concentration. After deriving the flux and concentration equations, the numerical implementation in the commercial finite element solver ABAQUS is discussed. This is achieved through the user-defined UMATHT subroutine by exploiting the analogy between heat transfer equations and the hydrogen transport formulation.

2.3.1 Lattice Diffusion of Hydrogen

Lattice diffusion of the hydrogen is forced by a chemical potential gradient $\nabla\mu$. Onsager coefficients (L_{ij}) relate the chemical potential gradient ($\nabla\mu$) to the mass flux ($\mathbf{J}_i$) by the following relation:

$$\mathbf{J}_i = -\sum_{j=1}^{n} L_{ij}\nabla\mu_j \tag{2.29}$$

Note that the minus sign in the equation indicates that the hydrogen atoms moves from regions of high chemical potential to regions of low chemical potential. If only fluxes between lattice sites are to be considered, Equation 2.29 reduces to:

$$\mathbf{J}_L = -L_{LL}\nabla\mu_L \tag{2.30}$$

In this thesis, it is assumed that fluxes between trapping sites can be neglected due to their deep potential energy preventing diffusion between these sites. Consequently, the total flux ($\mathbf{J}$) is considered to be solely the flux between lattice sites ($\mathbf{J}_L$), so $\mathbf{J} \equiv \mathbf{J}_L$ and $\mu \equiv \mu_L$. The coefficient of Onsager is related to the diffusion equation of the Einstein through:

$$L_{LL} = \frac{D}{RT} C_L \tag{2.31}$$

where D is the coefficient of diffusion, R is the gas constant, T is temperature and C_L is the lattice concentration of the hydrogen atoms.

One can drive the equation of chemical potential of the hydrogen by assuming a following free energy function for the chemo-elastic energy stored in the bulk material [107]:

$$\psi^c(C) = \mu^0 C + RTN \left(\theta_L \ln \theta_L + (1 - \theta_L) \ln(1 - \theta_L)\right) \tag{2.32}$$

Then, the chemical potential can be expressed using the relationship between occupancy (θ_L), number of lattice sites per unit volume (N) and the lattice concentration of the hydrogen (C), $C = N_L \theta_L$ [108], as follows:

$$\mu = \frac{\partial \Psi^c(C)}{\partial C} = \mu^0 + RT \ln \frac{\theta_L}{1 - \theta_L} - \overline{V}_H \sigma_H \tag{2.33}$$

where σ_H is the hydrostatic stress, μ^0 is the standard state chemical potential, and $\overline{V}_H$ is the partial molar volume of hydrogen. The term with hydrostatic stress as a multiplier in Equation 2.33 refers to the stress-dependent component of the chemical potential, coupling the chemical potential of the diffusion problem to the deformation problem.

The total flux of the hydrogen diffusion can be readily obtained by substituting 2.33 and 2.31 into 2.30:

$$\mathbf{J} = -D \frac{C_L}{1 - \theta_L} \left(\frac{\nabla C_L}{C_L} - \frac{\nabla N_L}{N_L} \right) + \frac{D}{RT} C_L \overline{V}_H \nabla \sigma_H \tag{2.34}$$

Rearranging the expression, assuming the concentration of the interstitial lattice sites is constant over the spatial domain ($\nabla N_L = 0$) and low occupancy of hydrogen ($\theta_L \ll 1$), yields:

$$\mathbf{J} = -D \nabla C_L + \frac{D}{RT} C_L \overline{V}_H \nabla \sigma_H \tag{2.35}$$

The derivative of the total flux with respect to the lattice concentration of hydrogen, which will be used later in the Subsection 2.3.3.1, can be easily obtained as follows:

$$\frac{\partial \mathbf{J}}{\partial C_L} = \frac{D}{RT}\overline{V}_H \nabla \sigma_H \tag{2.36}$$

2.3.2 Mass Balance

The mass balance equation relates the change in hydrogen concentration to the flux resulting from the chemical potential gradient whose formulation is presented in Subsection 2.3.1. Consider a solid body Ω with an external surface $\partial\Omega$, which consists of a region where the flux is prescribed, $\partial\Omega_q$ (Neumann-type boundary conditions), and a region where the hydrogen concentration is prescribed, $\partial\Omega_C$ (Dirichlet-type boundary conditions), as illustrated in Figure 2.4. Then, the hydrogen flux exiting Ω through the external surface $\partial\Omega_q$ with outward normal $\mathbf{n}$ can be expressed as $q = \mathbf{J} \cdot \mathbf{n}$.

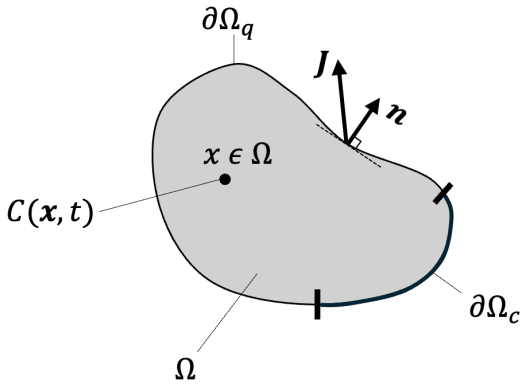

Figure 2.4: Schematic representation of the boundary value problem for the mass transport

By applying the mass balance requirements, the following governing equation for the conservation of mass can be written:

$$\int_\Omega \frac{dC}{dt}\, dV + \int_{\partial\Omega} \mathbf{J} \cdot \mathbf{n}\, dS = 0 \tag{2.37}$$

Applying the divergence theorem to Equation 2.37, and noting that the above equality must hold for any volume, the strong form of the mass balance equation is obtained:

$$\frac{dC}{dt} + \nabla \cdot \mathbf{J} = 0 \tag{2.38}$$

By substituting Equation 2.35 from Subsection 2.3.1 into Equation 2.38, the hydrogen transport equation can be obtained as follows:

$$\frac{\partial C_L}{\partial t} = D\nabla^2 C_L - \nabla\left(\frac{DC_L}{RT}\overline{V}_H \nabla\sigma_H\right) \tag{2.39}$$

2.3.3 Numerical Implementation of the Hydrogen Transport Model

This subsection details the analogy between heat transfer and hydrogen transport equations, which enables the use of the UMATHT subroutine in ABAQUS to define the constitutive relations for stress-assisted hydrogen diffusion. A critical parameter in this calculation is the hydrostatic stress gradient, which links the coupling between hydrogen diffusion and mechanical deformation. The manipulation of UMATHT through this analogy is explained, and the subsection concludes with a discussion on the numerical calculation of the hydrostatic stress gradient.

2.3.3.1 Heat Transfer Analogy

The hydrogen transport equations derived in Subsections 2.3.1 and 2.3.2 are implemented in ABAQUS by exploiting the analogy between heat transfer and mass transport equations. This approach enables the use of the UMATHT user-defined subroutine to simulate hydrogen transport within the coupled framework of deformation, mass transport, and fracture problems. Remember the energy balance equation for a stationary solid without any heat source:

$$\frac{d}{dt}\int_V \rho e \, dV = \int_S \mathbf{J} \, dS \tag{2.40}$$

By applying the divergence theorem:

$$\rho\dot{e} = -\nabla \cdot \mathbf{J} \tag{2.41}$$

where $\mathbf{J}$ is the heat flux vector, which depends on the temperature gradient according to Fourier's law, e is the internal energy per unit mass, and ρ is the density of the solid. Remember that at constant pressure, internal energy per unit mass can be expressed using the specific heat capacity (c_p) and temperature (T) as follows:

$$e = c_p T, \quad \dot{e} = c_p \dot{T} \tag{2.42}$$

Rewriting Equation 2.42 into Equation 2.41, following expression is obtained:

$$\rho c_p \frac{\partial T}{\partial t} + \nabla \cdot \mathbf{J} = 0 \tag{2.43}$$

Table 2.1 compares the equations obtained in Subsection 2.3.2 with those in this section to highlight the analogy between the hydrogen transport equations and heat transfer equations.

Table 2.1: Analogy between heat transfer and hydrogen transport equations

	Heat Transfer	Hydrogen Transport
Strong Form	$\rho c_p \frac{\partial T}{\partial t} + \nabla \cdot \mathbf{J} = 0$	$\frac{\partial C}{\partial t} + \nabla \cdot \mathbf{J} = 0$
Evolution Equation	$\dot{e} = c_p \dot{T}$	$\dot{C} = \dot{C}_L$
Degree of Freedom	T	C_L
Flux	$\mathbf{J}$	$\mathbf{J}$
Heat Capacity	c_p	1
Density	ρ	1

2.3.3.2 Calculation of the Gradient of Hydrostatic Stress

To compute the diffusion flux of the hydrogen given in Equation 2.35, it is necessary to determine the gradient of the hydrostatic stress. For this purpose, a numerical differentiation method is employed, which uses the integration point values of the hydrostatic stress multiplied by the derivatives of the shape functions. On the other hand, since the 3D brick element (C3D8) used in this thesis is linear, the integration point values of the hydrostatic stress within a single element are all the same. Therefore, gradient calculations based solely on the integration point values within one element result in a zero gradient. To address this, the effects of neighboring elements should be included in the gradient calculations. Moreover, by incorporating the effects of neighboring elements into the calculation of the hydrostatic stress gradient, the framework extends from being purely local to nonlocal. This approach results in a smoother gradient of the hydrostatic stress when moving from one element to another, more accurately representing the physical phenomena. Additionally, reducing sudden jumps in the hydrostatic stress gradient values enhances the computational stability

of the finite element model. Nonlocality is introduced through nodal averaging, as illustrated in a two-dimensional, 4-node, 4-integration point element in Figure 2.5.

The process of nodal averaging can be outlined as follows:

- First, the constitutive model, implemented in ABAQUS through the UMAT subroutine as mentioned in Section 2.1, solves the deformation problem and returns the stress and strain values at the current time increment. These values are stored for all integration points and passed to the UMATHT subroutine for the calculation of the hydrostatic stress gradient.

- Hydrostatic stress at all integration points is calculated based on its definition at the same time increment as the stress tensor computed by the UMAT subroutine:

$$\sigma_H = \frac{I_i}{3} = \frac{1}{3}\,\mathrm{tr}(\sigma) \tag{2.44}$$

- The obtained values of hydrostatic stress are then extrapolated to each node of the element using the inverse of the shape functions. For example, consider the concurrent node i shared by four elements: a, b, c, and d. The contribution of the hydrostatic stress at node i from element a, denoted by σ_H^a, is computed as follows:

$$\sigma_H = \sum_{j=1}^{4} N_j'(x_i, y_i)(\sigma_H)_j \tag{2.45}$$

  Here, j represents the index for the integration point, and x_i and y_i are the x and y coordinates of node i. Similar calculations are performed to compute the contributions of elements b, c, and d to node i, denoted by σ_H^b, σ_H^c, and σ_H^d, respectively.

- After obtaining σ_H^a, σ_H^b, σ_H^c, and σ_H^d—the contributions of each element to the concurrent node i—their values are averaged to obtain a single nodal value of σ_H:

$$\sigma_H = \frac{\sigma_H^a + \sigma_H^b + \sigma_H^c + \sigma_H^d}{4} \tag{2.46}$$

- This nodal averaged value of hydrostatic stress is then interpolated back to the integration points using the shape functions to obtain the updated hydrostatic

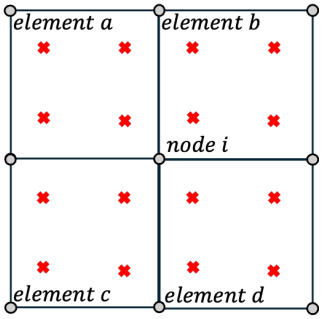

(a)

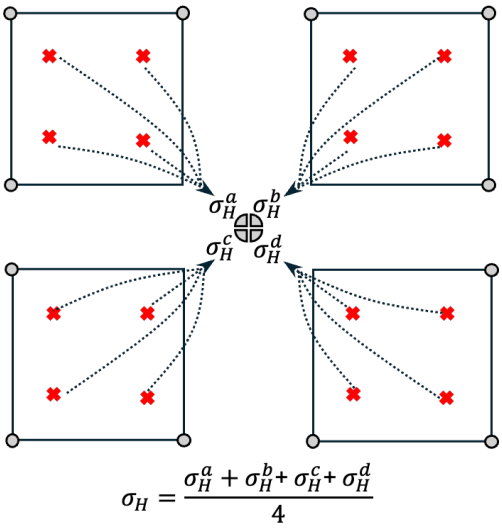

(b)

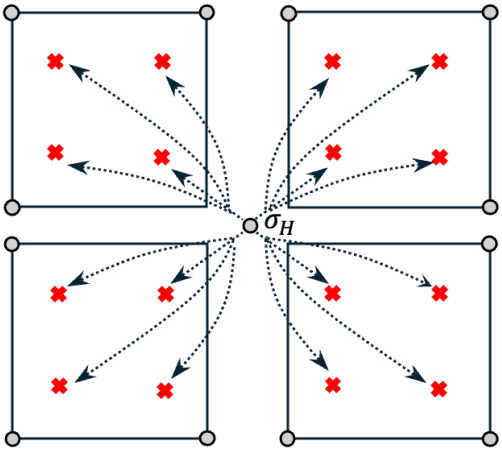

(c)

Figure 2.5: Schematic representation of the nodal averaging

stress values at the integration points of each element:

$$\sigma_H = \sum_{i=1}^{4} N_i(x_j, y_j)(\sigma_H)_i \tag{2.47}$$

Here, i represents the index of the nodes, while x_j and y_j are the x and y coordinates of the integration points.

The above procedure is generalized in the UMATHT subroutine to automatically identify each concurrent node and neighboring element, allowing for the computation of the hydrostatic stress value at each integration point within the three-dimensional 8-node, 8-integration point finite element domain.
The gradient calculation proceeds at the element level as follows:

- For the linear brick element shown in Figure 2.6, adopted linear shape functions are given in Table 2.2. N_i is the shape function for node i, and ξ, η, and ρ are the coordinates in the isoparametric space.

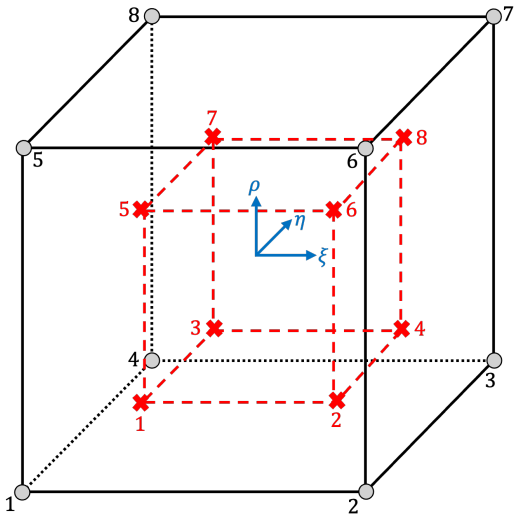

Figure 2.6: Visualization of an 8-node, 8-integration point brick element (C3D8)

- The relationship between the global coordinates and the isoparametric coordi-

Table 2.2: Adopted shape functions

Node i	N_i
1	$0.125(1-\xi)(1-\eta)(1-\rho)$
2	$0.125(1+\xi)(1-\eta)(1-\rho)$
3	$0.125(1+\xi)(1+\eta)(1-\rho)$
4	$0.125(1-\xi)(1+\eta)(1-\rho)$
5	$0.125(1-\xi)(1-\eta)(1+\rho)$
6	$0.125(1+\xi)(1-\eta)(1+\rho)$
7	$0.125(1+\xi)(1+\eta)(1+\rho)$
8	$0.125(1-\xi)(1+\eta)(1+\rho)$

nates can be expressed as:

$$\begin{aligned} x &= \sum_{k=1}^{8} N_k(\xi,\eta,\rho)x_k \\ y &= \sum_{k=1}^{8} N_k(\xi,\eta,\rho)y_k \\ z &= \sum_{k=1}^{8} N_k(\xi,\eta,\rho)z_k \end{aligned} \tag{2.48}$$

where x_k, y_k, and z_k are the coordinates of the Gauss points, as listed in Table 2.3.

- Using the integration point values of the hydrostatic stress, the distribution of the hydrostatic stress within the element can be expressed using the shape functions provided in Table 2.2 as follows:

$$\sigma_H = \sum_{k=1}^{8} N_k(\xi,\eta,\rho)(\sigma_H)_k \tag{2.49}$$

- The derivatives of the shape functions in the isoparametric domain are given in Table 2.4

- The derivatives of the shape functions in the global coordinates can be related to their derivatives in the isoparametric coordinates through the Jacobian as

Table 2.3: Gauss points

k	x_k	y_k	z_k
1	$-1/\sqrt{3}$	$-1/\sqrt{3}$	$-1/\sqrt{3}$
2	$1/\sqrt{3}$	$-1/\sqrt{3}$	$-1/\sqrt{3}$
3	$-1/\sqrt{3}$	$1/\sqrt{3}$	$-1/\sqrt{3}$
4	$1/\sqrt{3}$	$1/\sqrt{3}$	$-1/\sqrt{3}$
5	$-1/\sqrt{3}$	$-1/\sqrt{3}$	$1/\sqrt{3}$
6	$1/\sqrt{3}$	$-1/\sqrt{3}$	$1/\sqrt{3}$
7	$-1/\sqrt{3}$	$1/\sqrt{3}$	$1/\sqrt{3}$
8	$1/\sqrt{3}$	$1/\sqrt{3}$	$1/\sqrt{3}$

Table 2.4: Derivatives of the adopted shape functions

Node i	$\partial N_i/\partial\xi$	$\partial N_i/\partial\eta$	$\partial N_i/\partial\rho$
1	$-0.125(1-\eta)(1-\rho)$	$-0.125(1-\xi)(1-\rho)$	$-0.125(1-\xi)(1-\eta)$
2	$0.125(1-\eta)(1-\rho)$	$-0.125(1+\xi)(1-\rho)$	$-0.125(1+\xi)(1-\eta)$
3	$-0.125(1+\eta)(1-\rho)$	$0.125(1-\xi)(1-\rho)$	$-0.125(1-\xi)(1+\eta)$
4	$0.125(1+\eta)(1-\rho)$	$0.125(1+\xi)(1-\rho)$	$-0.125(1+\xi)(1+\eta)$
5	$-0.125(1-\eta)(1+\rho)$	$-0.125(1-\xi)(1+\rho)$	$0.125(1-\xi)(1-\eta)$
6	$0.125(1-\eta)(1+\rho)$	$-0.125(1+\xi)(1+\rho)$	$0.125(1+\xi)(1-\eta)$
7	$-0.125(1+\eta)(1+\rho)$	$0.125(1-\xi)(1+\rho)$	$0.125(1-\xi)(1+\eta)$
8	$0.125(1+\eta)(1+\rho)$	$0.125(1+\xi)(1+\rho)$	$0.125(1+\xi)(1+\eta)$

follows:

$$J \begin{bmatrix} \partial N_k/\partial x \\ \partial N_k/\partial y \\ \partial N_k/\partial z \end{bmatrix} = \begin{bmatrix} \partial N_k/\partial \xi \\ \partial N_k/\partial \eta \\ \partial N_k/\partial \rho \end{bmatrix} \tag{2.50}$$

where Jacobian is defined as:

$$J = \frac{\partial(x,y,z)}{\partial(\xi,\eta,\rho)} = \begin{bmatrix} \partial x/\partial\xi & \partial y/\partial\xi & \partial z/\partial\xi \\ \partial x/\partial\eta & \partial y/\partial\eta & \partial z/\partial\eta \\ \partial x/\partial\rho & \partial y/\partial\rho & \partial z/\partial\rho \end{bmatrix} = \begin{bmatrix} \sum_{k=1}^{8} \frac{\partial N_k}{\partial\xi} x_k & \sum_{k=1}^{8} \frac{\partial N_k}{\partial\xi} y_k & \sum_{k=1}^{8} \frac{\partial N_k}{\partial\xi} z_k \\ \sum_{k=1}^{8} \frac{\partial N_k}{\partial\eta} x_k & \sum_{k=1}^{8} \frac{\partial N_k}{\partial\eta} y_k & \sum_{k=1}^{8} \frac{\partial N_k}{\partial\eta} z_k \\ \sum_{k=1}^{8} \frac{\partial N_k}{\partial\rho} x_k & \sum_{k=1}^{8} \frac{\partial N_k}{\partial\rho} y_k & \sum_{k=1}^{8} \frac{\partial N_k}{\partial\rho} z_k \end{bmatrix} \tag{2.51}$$

- Finally, the spatial gradient of the hydrostatic stress is found as:

$$\begin{aligned} (\nabla\sigma_H)_x &= \sum_{i=1}^{8} \frac{\partial N_i}{\partial x} (\sigma_H)_i \\ (\nabla\sigma_H)_y &= \sum_{i=1}^{8} \frac{\partial N_i}{\partial y} (\sigma_H)_i \\ (\nabla\sigma_H)_z &= \sum_{i=1}^{8} \frac{\partial N_i}{\partial z} (\sigma_H)_i \end{aligned} \tag{2.52}$$

2.4 Numerical Coupling of the Framework

The details of the numerical coupling framework are provided in this section. The mechanical behavior of the material is defined using the ABAQUS user subroutine UMAT, where the constitutive equations of the material are specified, as detailed in Section 2.1. The Park-Paulino-Roesler (PPR) cohesive zone model, detailed in Section 2.2, is implemented in the UEL subroutine to simulate intergranular crack initiation and propagation under the influence of hydrogen. The constitutive equations for hydrogen diffusion due to the chemical potential gradient, whose details are given in Section 2.3, are implemented through the UMATHT user subroutine, utilizing the analogy between heat transfer and hydrogen transport equations. The framework is coupled such that mechanical deformation drives the transport of hydrogen through the dependency of chemical potential on pressure, as summarized in Figure 2.7.

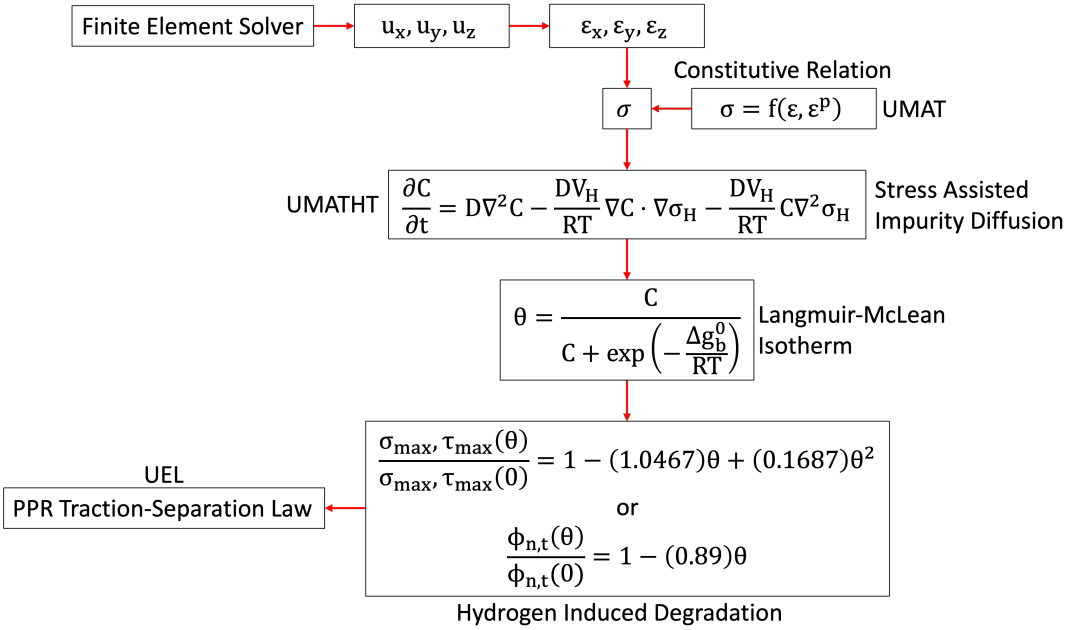

Figure 2.7: Flowchart of the coupled framework

2.4.1 The Effect of Hydrogen on Failure through Cohesive Zone Elements

As hydrogen diffuses from low-pressure to high-pressure regions, it accumulates in the intergranular fracture process zones, where both the gradients of hydrostatic stress and the hydrostatic stress itself are already high. The influence of hydrogen on crack initiation and propagation is facilitated by coupling the PPR cohesive zone model parameters with the surface coverage of hydrogen, calculated from the bulk concentration of hydrogen using the Langmuir-Mclean isotherm [109] as follows:

$$\theta = \frac{C}{C + \exp\left(\frac{-\Delta g_b^0}{RT}\right)} \tag{2.53}$$

where C is the concentration of hydrogen given in units of impurity mole fraction, Δg_b^0 is the Gibbs free energy difference between the debonding surface and the surrounding, R is the gas constant, and T is the temperature.

There exist literature findings that relate both the cohesive strength (σ_{max}, τ_{max}) and fracture energy (ϕ_n, ϕ_t) to the surface coverage of hydrogen (θ). [110] uses density functional theory (DFT) to calculate the fracture energy and its variation from first principles for two metals, iron (Fe) and aluminum (Al), in the presence of varying hydrogen concentrations. [111] builds upon the findings of [110] and suggests that

the cohesive strength of iron is related to hydrogen surface coverage through the following relation:

$$\frac{\sigma_{max}(\theta)}{\sigma_{max}(0)} = 1 - (1.0467)\theta + (0.1687)\theta^2 \tag{2.54}$$

where $\sigma_{max}(0)$ represents the cohesive strength without hydrogen influence and θ is the hydrogen surface coverage as defined in Equation 2.53.
[39] utilizes the surface energy data from [110] to propose a simple linear fit for the variation of the fracture energies of the two materials as a function of the hydrogen surface coverage values, as follows:
For Fe:

$$\frac{\phi_n(\theta)}{\phi_n(0)} = 1 - (0.89)\theta \tag{2.55}$$

For Al:

$$\frac{\phi_n(\theta)}{\phi_n(0)} = 1 - (0.67)\theta \tag{2.56}$$

where $\phi_n(\theta)$ is the fracture energy under the influence of the hydrogen, $\phi_n(0)$ is the fracture energy without the effect of hydrogen and θ is the surface coverage of the hydrogen.

[112] combines density functional theory (DFT) with the finite element method and utilizes nanoscale experiments to derive a relation for the fracture energy of nickel (Ni) with respect to hydrogen surface coverage (θ). Following the approach used for Fe and Al, [39] provides a linear fit for the fracture energy of Ni as follows:

$$\frac{\phi_n(\theta)}{\phi_n(0)} = 1 - (0.41)\theta \tag{2.57}$$

Figure 2.8 presents the experimental findings for iron and aluminum from [110], and nickel from [112], along with the curve fits from [39].

The provided relations for both cohesive strength (σ_{max}, τ_{max}) and fracture energy (ϕ_n, ϕ_t) incorporate the effect of hydrogen into failure modelling. The hydrogen concentration at the nodes connecting to the cohesive zone elements directly affects the input parameters of each cohesive element. As the hydrogen concentration increases, either the cohesive strength or the fracture energy is decreased, which facilitates crack propagation due to the buildup of hydrogen.

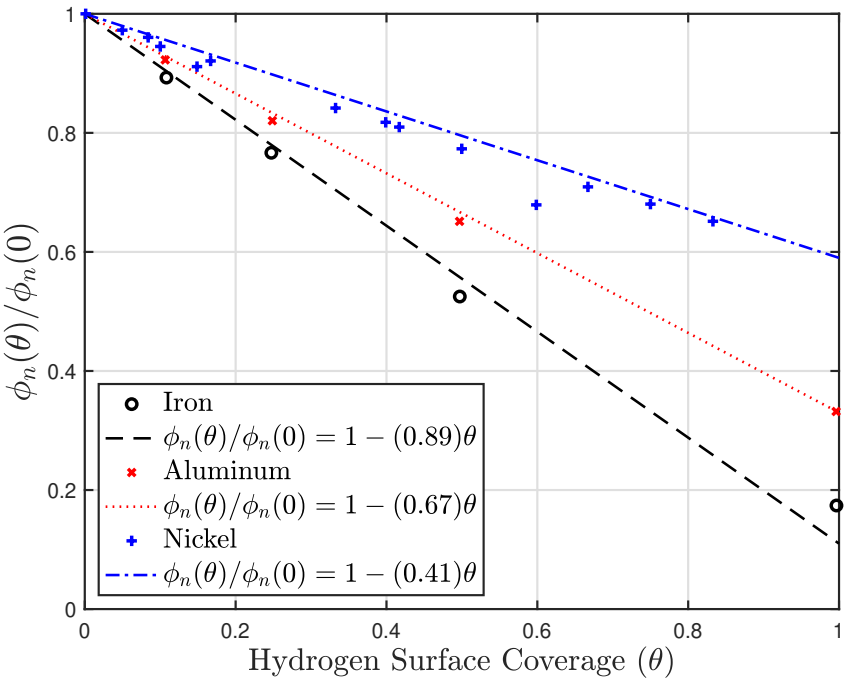

Figure 2.8: Variation of fracture energy with hydrogen surface coverage for iron, aluminum and nickel

2.4.2 Implementation of the Framework using ABAQUS User Subroutines

This subsection details the implementation of the coupled framework for deformation, mass transport, and failure analysis using the user subroutines utilized in the commercial finite element solver software ABAQUS. The constitutive equations are managed by five ABAQUS subroutines: UMAT, UMATHT, UEL, UEXTERNALDB, and URDFIL.

The UMAT subroutine is called at every integration point of the bulk elements for all time steps of the simulation to solve the constitutive equations for mechanical deformation and to obtain the stress and solution-dependent state variables. To calculate the mass flux in the hydrogen diffusion problem, it is necessary to determine the gradient of the hydrostatic stress, as shown in Equation 2.35. To achieve this, the module block in FORTRAN programming language is used to store hydrostatic stress results at the end of each time increment. Using the module block, a database of stored variables can be created, which can be accessed by other user subroutines. After each

call to the UMAT subroutine at an integration point during the simulation, σ_H values are recorded into this database. Once calculations are completed for all integration points at the end of each time increment, the gradient of hydrostatic stress is ready to be calculated.

The UEL subroutine is called for each cohesive zone element to calculate the separation at every time increment based on the defined traction-separation law, using the model parameters detailed in Section 2.2.

The UEXTERNALDB subroutine is utilized for operations concerning the entire finite element domain, rather than only an individual element. At the very beginning of the analysis, this subroutine is called to store the nodal connectivity of both bulk and cohesive zone elements to be used in the gradient calculations. At the end of the first increment, using the obtained hydrostatic stress values from the UMAT subroutine, this subroutine is called again to apply the nodal averaging scheme for hydrostatic stress, as detailed in Subsection 2.3.3.2. After applying the averaging scheme to all elements and updating the integration point values of the hydrostatic stress, the gradient of the hydrostatic stress at each integration point is calculated with the help of the derivative of the shape functions, as detailed in Subsection 2.3.3.2. These gradient values are stored in the module block to be used as input for the constitutive equations in the hydrogen transport problem for the next time increment. It should be noted that since the calculated values of the hydrostatic stress gradient are used in each subsequent time increment for flux calculations in mass transport, the coupling of the mechanical deformation and hydrogen transport problems is considered explicit, and the solution type is staggered. For the subsequent time increments, with the hydrostatic stress gradients available from the previous increments, the constitutive equations for hydrogen transport can be solved in the UMATHT subroutine, allowing the hydrogen concentration at each integration point to be updated.

Finally, the URDFIL subroutine is used to read the current hydrogen concentration values at the nodes. Although ABAQUS can record the deformation history in an .ODB results file, accessing this file during the solution is impractical. Instead, by adding a nodal output request in the input file, the user can instruct ABAQUS to generate a .fil file in ASCII format. This format allows for faster read and write

operations compared to the .ODB file. The URDFIL subroutine can then access the .fil file to retrieve nodal hydrogen concentration information. These nodal values of hydrogen concentration are then used to couple the hydrogen transport problem with the failure analysis. As the nodal connectivity of the cohesive zone elements is read from the input file at the beginning of the analysis, and the nodal values of hydrogen concentration are read from the .fil file, the values at the nodes of each cohesive zone element can be averaged to assign a unique hydrogen concentration value to each element. Equation 2.53 is then used to calculate the surface coverage of hydrogen for each cohesive zone element. The resulting values are used to apply degradation to either the cohesive strength or fracture energy in the model parameters of traction-separation law of the PPR cohesive zone model, as explained in Subsection 2.4.1. As a result, the hydrogen transport and failure frameworks also become coupled. Figure 2.9 summarizes the framework in a flowchart to better visualize the procedure.

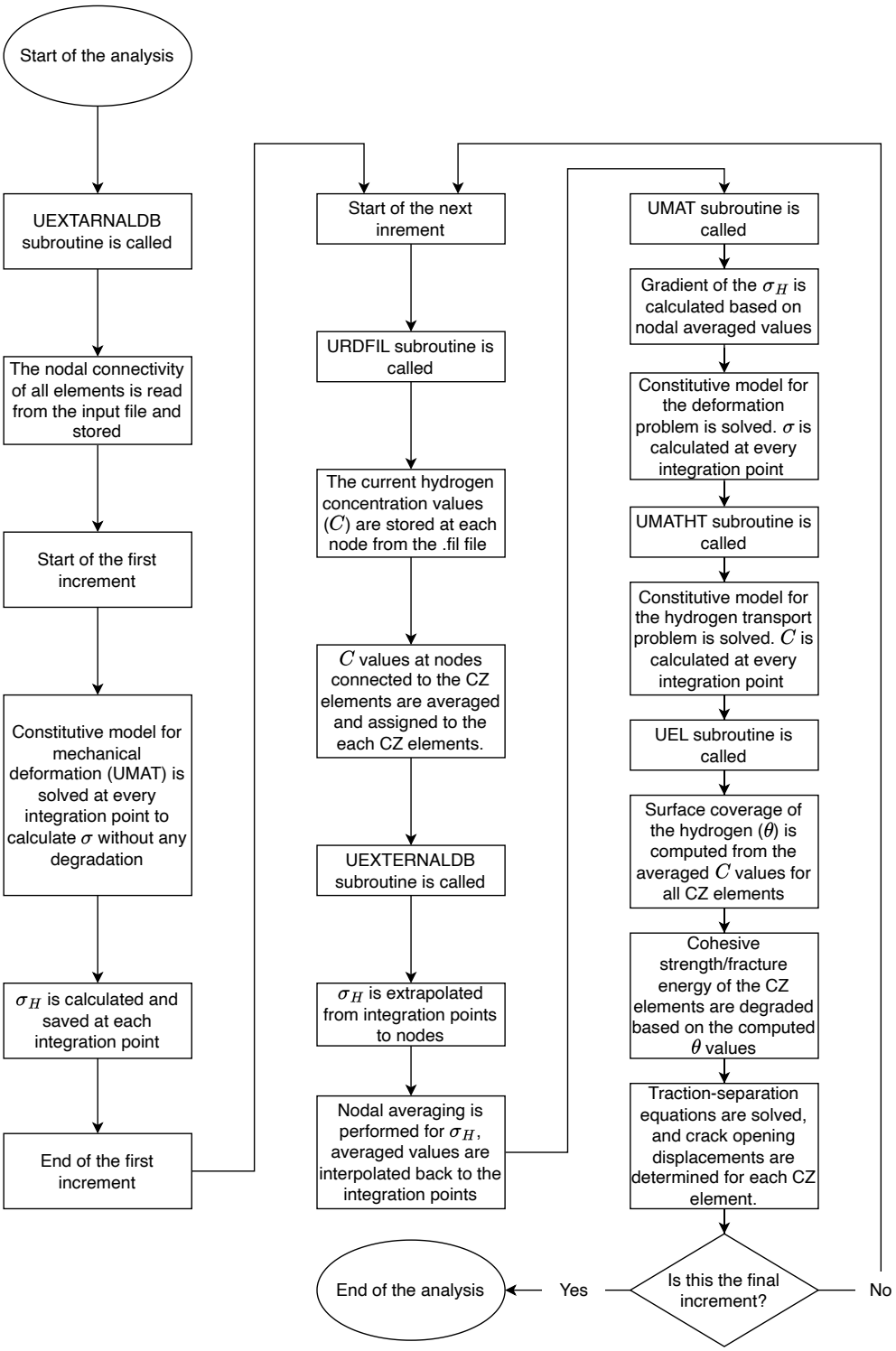

Figure 2.9: Flowchart of the coupled framework

CHAPTER 3

NUMERICAL FINDINGS

This section offers a detailed explanation of micromechanical modelling of failure influenced by hydrogen. The primary goal is to explore how microstructural characteristics impact the macroscopic behavior of the material using crystal plasticity formulations, while also investigating size effects through strain gradient crystal plasticity. To this end, two polycrystalline RVEs are generated: one with 50 grains and another with 350 grains. Simulations are conducted using the specified constitutive laws, with the transition from microscale to macroscale behavior achieved through a homogenization approach [113, 114].

The hydrogen-enhanced decohesion (HEDE) intergranular failure mechanism is modeled using 3D, generic yet realistic polycrystalline RVEs. Grain boundary separations are simulated through cohesive zone modelling, a well-established framework in the literature for capturing decohesion. For prior work by the author on micromechanical failure modelling in dual-phase steels utilizing the same cohesive zone formulation, refer to [115, 116, 117]. The RVEs are generated using a Voronoi tessellation algorithm, with cohesive zone elements—governed by a pre-defined potential based traction-separation law—inserted via an in-house script.

The following subsections detail the numerical modelling approaches utilized in the coupled framework. It begins with an explanation of the process for generating polycrystalline RVEs, followed by a discussion of the preprocessing scripts used to insert cohesive zone elements at grain boundaries and define contact between adjacent grain surfaces, allowing hydrogen diffusion across grains. The boundary conditions applied to maintain constant stress triaxiality during uniaxial loading simulations are also described. Additionally, the volumetric homogenization scheme is introduced,

alongside the simulation results for both two-dimensional notched specimens—used to validate the model with experimental data—and three-dimensional RVEs, which explore the micromechanics of hydrogen-induced failure.

3.1 Numerical Modelling

This subsection details the representative volume elements, the in-house scripts used to preprocess the simulation input files, and the boundary conditions applied for the polycrystalline RVE simulations. Furthermore, the algorithm employed to derive the macroscopic material response from the mesoscale RVE simulation results is also explained.

3.1.1 Representative Volume Elements

Representative Volume Elements (RVEs) play a crucial role in the study of heterogeneous materials by linking microscopic characteristics to macroscopic properties. An RVE is a small, statistically representative portion of a material that captures the key features of its microstructure. RVEs are designed to be sufficiently large to reflect the material's microstructure while remaining small enough for analytical or numerical analysis. Therefore, if there is significant mismatch or anisotropy in the material properties, the RVE needs to be sufficiently large to account for it. For instance, in polycrystalline materials, the RVE should include enough grains to ensure that the material's behavior remains consistent, even with a random distribution of crystallographic orientations. By employing this modelling technique, the material's response can be simulated without the need for full-scale modelling, significantly reducing computational costs. Accurately modelling an RVE enables simulations to predict how a material will perform under various conditions. This predictive capability facilitates the design and optimization of new materials. Additionally, RVEs help identify the impact of defects, inclusions, and other heterogeneities on the material's overall behavior.

Voronoi tessellation is a widely used and effective method for generating RVEs. This mathematical technique divides space into distinct regions based on proximity to a

set of seed points. In the tessellation, each seed point corresponds to a specific phase or grain within the material, resulting in a cell that represents its spatial distribution. Spherical growth is then initiated from the seed points, expanding until the RVE volume is fully filled. This approach is particularly useful for modelling polycrystalline materials, composites, and other heterogeneous materials with complex microstructures. The polycrystalline RVEs analyzed in this thesis are generated using the Voronoi tessellation generator software Neper [118]. Figure 3.1 shows an example of an RVE generated and meshed using Neper.

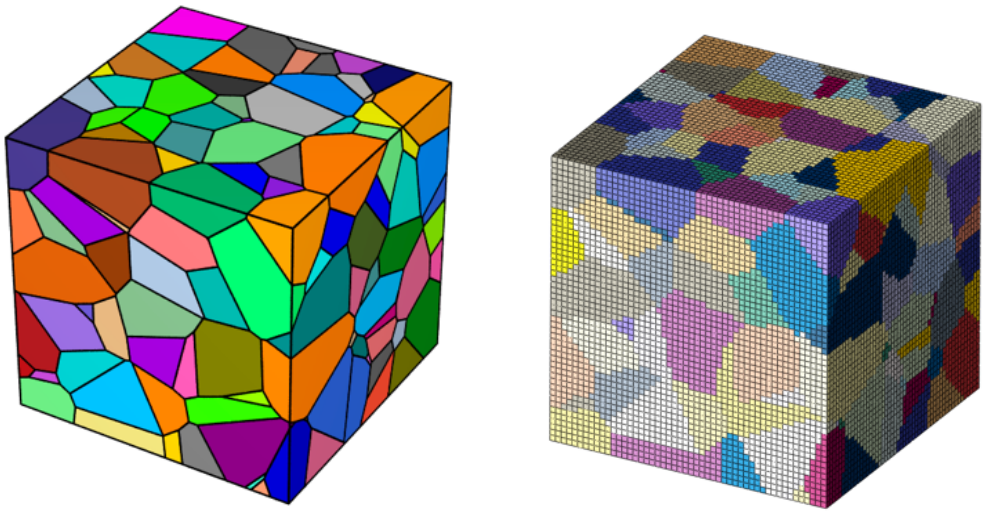

(a) (b)

Figure 3.1: Example of polycrystalline RVEs: Generated (a) and meshed (b) using Neper software.

3.1.2 Preprocessing of the Numerical Simulations

After generating the RVEs using the Voronoi tessellation algorithm (as explained in Subsection 3.1.1), cohesive zone elements are inserted using an in-house script. This script identifies the nodal connectivity in the original mesh, locates interface surfaces at grain boundaries, and inserts 8-node, zero-thickness linear cohesive zone elements (illustrated in Figure 2.2) between adjacent grains. An example of a 3D polycrystalline RVE with inserted cohesive zone elements is shown in Figure 3.2.

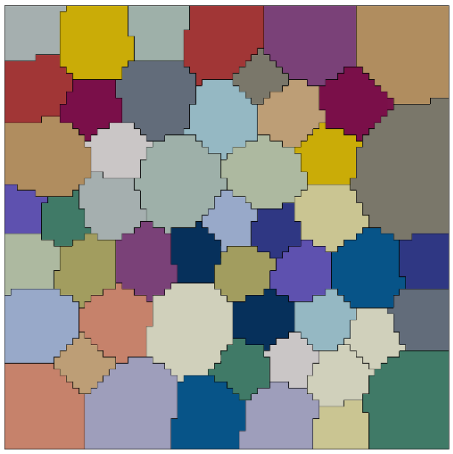

(a) Front view of the RVE

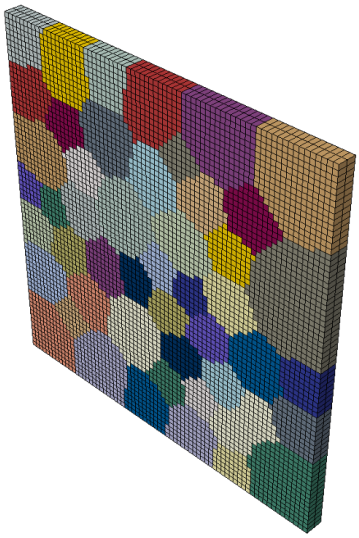

(b) Isometric view of the meshed RVE

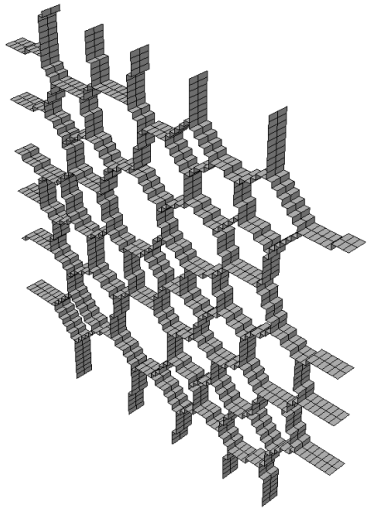

(c) Inserted cohesive zone elements

Figure 3.2: Visualization of an example polycrystalline RVE with cohesive zone elements at the grain boundaries

Once the cohesive zone elements are inserted between each grain boundary, an additional in-house preprocessing algorithm is run to define and create surface sets at the adjacent grain boundary surfaces. This step is necessary to allow hydrogen to diffuse between grains. Since cohesive zone elements are placed at all grain boundaries and the hydrogen diffusion algorithm is implemented using an analogy with the heat transfer problem via the UMATHT subroutine, only the bulk elements have nodal de-

grees of freedom for hydrogen concentration. The presence of cohesive zone elements restricts hydrogen diffusion between the grains they surround, as these elements do not possess nodal degrees of freedom for hydrogen concentration. To address this, the capabilities of the ABAQUS are utilized. The hydrogen diffusion problem is implemented within the numerical framework by exploiting the analogy between heat transfer and diffusion via the UMATHT subroutine. Thus, an external flux vector can be defined between the adjacent surfaces of each grain, which are separated by cohesive zone elements. The interaction properties are configured to allow infinite concentration flux from the master to slave surfaces by assigning the highest possible conductivity value that the compiler can interpret, effectively bypassing the cohesive zone elements, which would otherwise obstruct hydrogen diffusion due to the lack of nodal degrees of freedom for hydrogen concentration. An additional in-house preprocessing script is developed to automatically identify and define the respective master and slave surfaces. The script identifies elements that have surfaces at grain boundaries and locates their neighboring counterpart from the adjacent grain. It then creates an element set with consistent surface identifiers and defines the master and slave surfaces for each pair of neighboring elements at the grain boundaries.

3.1.3 Boundary Conditions

In numerical simulations using RVEs to model material responses, it's crucial to define a boundary value problem that accurately reflects the bulk material. Consequently, the boundary conditions and applied loads must closely match those of the experimental setup. In this thesis, the RVEs are subjected to uniaxial tensile loading. To accurately model this loading condition and maintain a consistent stress state throughout the analysis, determining the stress triaxiality under uniaxial tension is essential. Stress triaxiality, which measures the state of stress at a point within the material, is defined as the ratio of hydrostatic stress to the equivalent stress, as shown below:

$$T = \frac{\sigma_H}{\sigma_{eq}} \tag{3.1}$$

where,

$$\sigma_H = \frac{\sigma_x + \sigma_y + \sigma_z}{3} \tag{3.2}$$

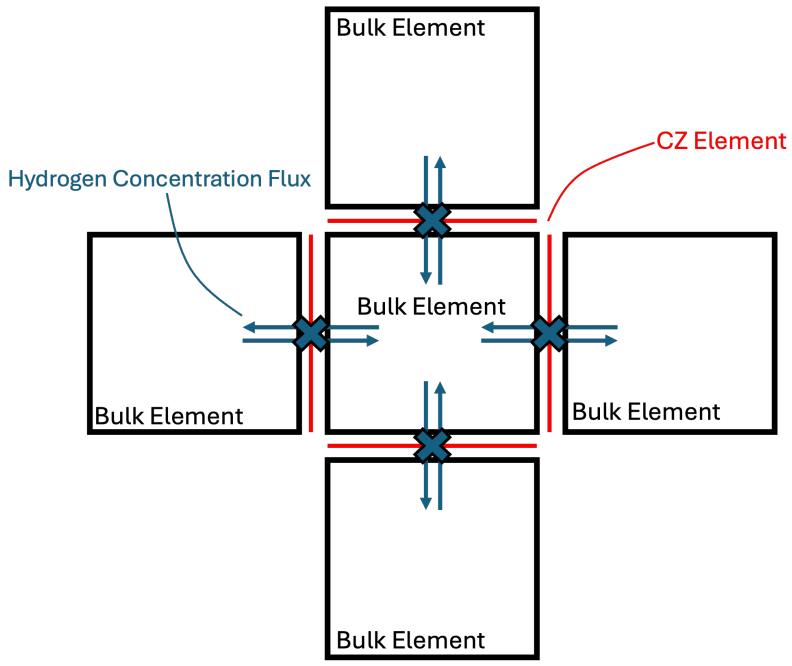

(a) Diffusion between adjacent bulk elements is limited by the presence of CZ elements

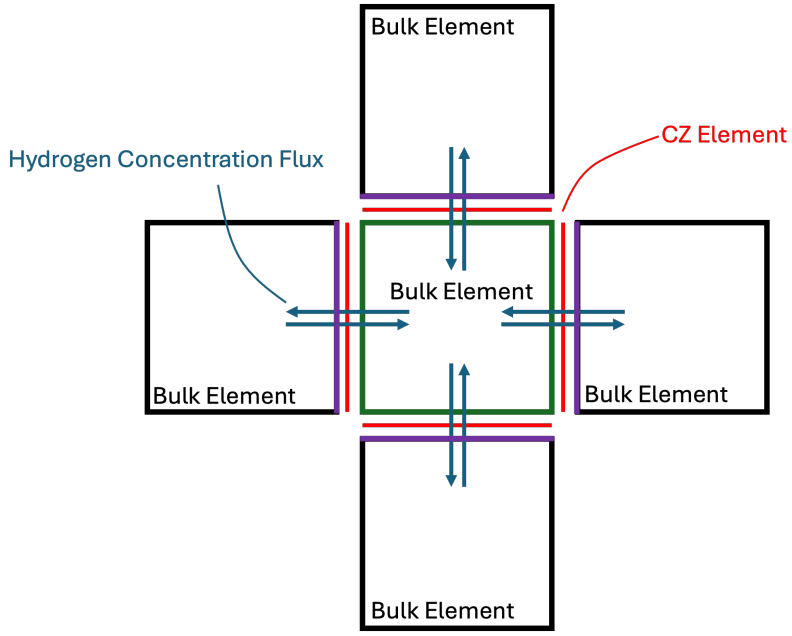

(b) Diffusion is facilitated through the defined master-slave contact surfaces

Figure 3.3: Illustration of the preprocessing steps enabling hydrogen diffusion through grain boundaries

and,

$$\sigma_{eq} = \frac{1}{\sqrt{2}}\sqrt{(\sigma_x - \sigma_y)^2 + (\sigma_x - \sigma_z)^2 + (\sigma_z - \sigma_y)^2} \tag{3.3}$$

Stress triaxiality is an important factor in understanding a material's susceptibility to ductile fracture under different loading conditions. In the case of uniaxial tensile loading, the stress state is defined by a single non-zero normal stress component, while the other normal stress and shear stress components are zero. Assuming σ_x is the only non-zero normal stress component, the hydrostatic and equivalent stresses in uniaxial tension simplify to:

$$\sigma_H = \frac{\sigma_x}{3} \tag{3.4}$$

and,

$$\sigma_{eq} = \sigma_x \tag{3.5}$$

As a result, the stress triaxiality under uniaxial tension is determined to be $T = 1/3$. In the numerical simulations, a constant stress triaxiality is maintained within the polycrystalline RVEs by applying a set of constraints and boundary conditions as outlined in [114]. A master node is positioned at (L_x, L_y, L_z), where L_x, L_y, and L_z represent the dimensions of the RVE in the x, y, and z directions, respectively. The displacements of this master node are then coupled with the corresponding surfaces of the RVE in each direction, as illustrated in Figure 3.7. The three constraint equations are set up to ensure that the surfaces at $x = L_x$, $y = L_y$, and $z = L_z$ move with the same displacement as the master node in the direction normal to each respective surface.

$$\begin{aligned} u_x(L_x, y, z) - u_x^M &= 0 \\ u_y(x, L_y, z) - u_y^M &= 0 \\ u_z(x, y, L_z) - u_z^M &= 0 \end{aligned} \tag{3.6}$$

where u_x, u_y, and u_z denote the displacements along the x, y, and z axes, respectively, for any point at the specified coordinates, and u_x^M, u_y^M, and u_z^M correspond to the displacements of the master node. The bottom, back, and left surfaces of the RVEs are constrained in their respective normal directions through the following boundary

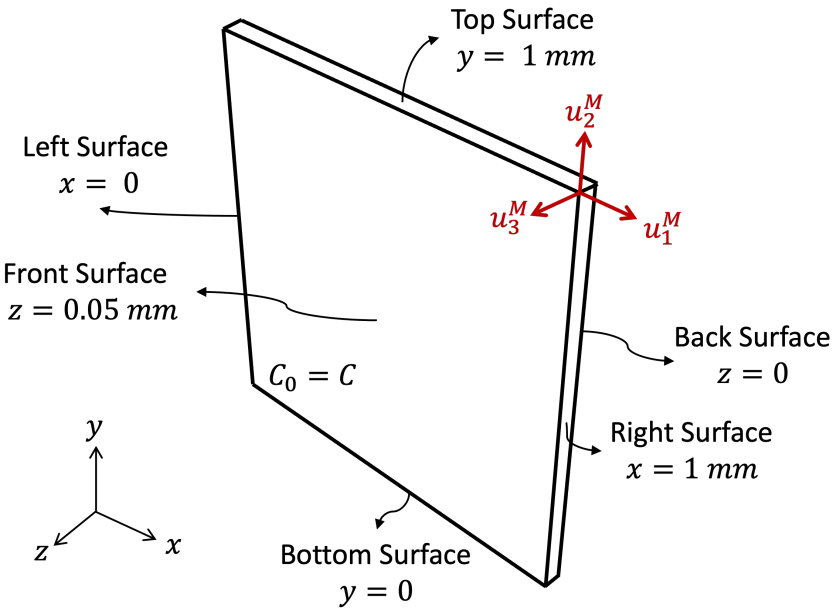

Figure 3.4: Schematic representation of an RVE illustrating the coordinate axes, surfaces, and the position of the master node.

conditions:

$$\begin{aligned} u_x(0, y, z) &= 0 \\ u_y(x, 0, z) &= 0 \\ u_z(x, y, 0) &= 0 \end{aligned} \tag{3.7}$$

In a uniaxial tension loading case with tension applied along the x-axis, only the displacement in the x-direction is prescribed to the master node. This allows the master node to move freely in the other two directions, while preventing rigid body motion of the RVE through the boundary conditions defined by Equation 3.7. As a result, the displacement applied to the master node is distributed across the RVE surfaces, ensuring a constant stress triaxiality of $T = 1/3$ throughout the uniaxial tension loading step applied. This is further confirmed using the volumetric averaging scheme presented in the next section, by verifying the ratio of the hydrostatic to equivalent homogenized stress values.

3.1.4 Homogenization

Homogenization is a computational method used to derive the macroscopic or mesoscopic behavior of a heterogeneous material based on its microscopic response. The macroscopic stress response of the material, Σ_{ij}, can be derived from the microscopic Cauchy stress components, σ_{ij}, as follows:

$$\Sigma_{ij} = \frac{1}{V} \int_V \sigma_{ij} dV \tag{3.8}$$

where $i, j = 1, 2, 3$ and V represents the current total volume of the RVE. Therefore, the stress components of each element within the RVE are integrated over the volume as follows:

$$\Sigma_{ij} = \frac{1}{V} \sum_{m=1}^{N} \left(\sum_{q=1}^{p} \sigma_{ij}^{q} v^{q} \right)^{m} \tag{3.9}$$

where N is the total number of elements, p is the total number of integration points per element, and v represents the volume of an integration point, which is updated continuously as deformation occurs throughout the simulation. The averaged strain components, E_{ij}, are calculated similarly by summing the microscopic strain components, ε_{ij}, for each element, weighted by their respective volumes. Given that ABAQUS outputs logarithmic strain, the resulting strain components are also in logarithmic form.

$$E_{ij} = \frac{1}{V} \sum_{m=1}^{N} \left(\sum_{q=1}^{p} \varepsilon_{ij}^{q} v^{q} \right)^{m} \tag{3.10}$$

where N is the total number of elements, p is the total number of integration points per element, and v represents the volume of an integration point.

3.2 Model Verification- Simulation of a Notched Round Bar Specimen

[58] presents an experimental study on high-strength AISI 4135 steel, using various notched cylindrical specimens subjected to tensile loading under different ambient hydrogen concentration levels. The study explores the relationship between notch tensile strength—defined as the ratio of the maximum tensile load during testing to the initial net cross-sectional area at the notch—and the diffusible hydrogen content. Experiments are conducted with three different notch radii: $\rho = 0.1$ mm, $\rho = 0.25$ mm,

and $\rho = 0.8$ mm, corresponding to calculated stress concentration factors of 4.9, 3.3, and 2.1, respectively. The notch radii of $\rho = 0.1$ mm and $\rho = 0.25$ mm are considered in the simulations for the verification. The experimental conditions are replicated using the numerical framework described in Chapter 2. The three-dimensional implementation outlined in the chapter is easily adaptable to a two-dimensional case by adjusting the relevant formulations, such as shape functions, to suit two-dimensional element types. The engineering stress-strain curves from the paper, without considering the influence of hydrogen, have been digitized and converted into true stress-strain data using the following formulations:

$$\begin{aligned} \varepsilon_{true} &= \ln(1 + \varepsilon_{eng}) \\ \sigma_{true} &= \sigma_{eng} e^{\varepsilon_{true}} = \sigma_{eng}(1 + \varepsilon_{eng}) \end{aligned} \tag{3.11}$$

The resulting true stress-strain curve is then utilized to fit the parameters of the isotropic Voce-type hardening law, which is expressed by the following equation:

$$\sigma = \sigma_y x_a \left(1 + \frac{E\varepsilon_p}{\sigma_y}\right)^N \tag{3.12}$$

where σ represents the flow stress, σ_y is the initial yield stress, x_a is a material parameter associated with the asymptotic hardening saturation value, E denotes the elastic modulus, ε_p is the equivalent plastic strain, and N is the hardening exponent. Obtained curve fit is given in Figure 3.5, with the following found model parameters:

$$\begin{aligned} \sigma_y &= 1235 \text{ MPa} \\ x_a &= 1.0146 \\ E &= 210000 \text{ MPa} \\ N &= 0.0592 \end{aligned} \tag{3.13}$$

The notched cylindrical bars with radii of $\rho = 0.1$ mm and $\rho = 0.25$ mm are modeled in ABAQUS. Cohesive zone elements are manually inserted along the symmetry axis of the geometry. Uniaxial tensile test simulations are performed with an engineering strain rate of $\dot{\varepsilon} = 8.3 \times 10^{-7}, \text{s}^{-1}$, as specified in the study. The diffusion-related material properties for AISI 4135 are provided as a partial molar volume of $\overline{V}_H = 2000, \text{mm}^3/\text{mol}$ and a diffusion coefficient of $D = 3.8 \times 10^{-5}, \text{mm}^2/\text{s}$. The notched cylindrical bars are precharged and tested under the same hydrogen environment, with hydrogen concentration levels ranging from 0.08 to 2.2 wt ppm. Similarly, for the

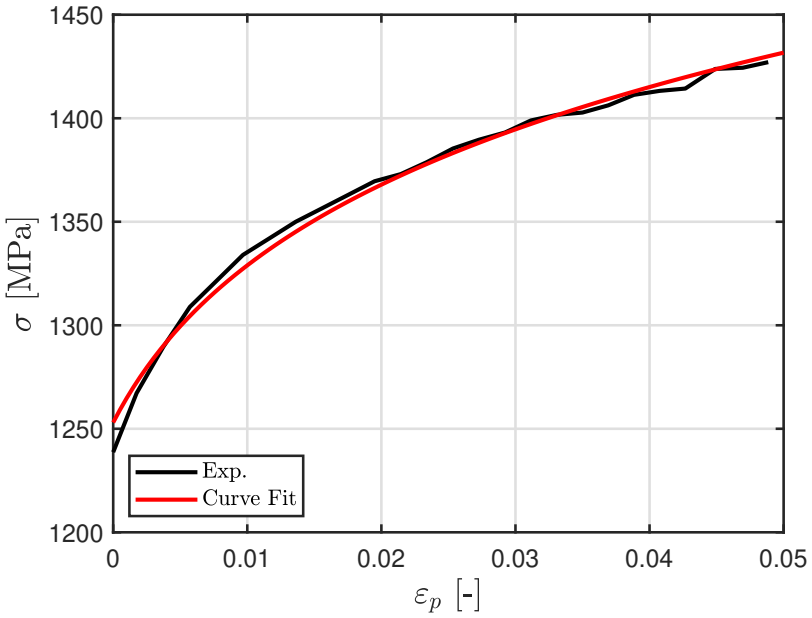

Figure 3.5: Fitted flow curve to the true stress-strain data obtained from [58]

simulations, the hydrogen concentration is assumed to be homogeneous throughout the entire specimen, with an initial condition applied to all nodes in the finite element domain. Since the specimens are exposed to ambient hydrogen at the same levels as in the precharging process during the experiments, hydrogen concentration boundary conditions are applied to the outermost surface nodes to replicate these experimental conditions. Figure 3.6 shows the specimen geometry used in the experiments, along with the 2D geometry and boundary and initial conditions of the simulated model, the mesh used, and the deformed shape at the end of the simulation. The bar is discretized using 16,541 four-node plane strain bulk elements and 100 four-node cohesive zone elements.

Figure 3.8 presents a comparison between the results obtained using the proposed framework, the experimental data from [58], and the numerical simulations from [39], which models hydrogen-induced fracture through a phase field fracture framework. The cohesive zone predictions show good agreement with the experimental data. As the precharged hydrogen concentration increases, the cohesive strength in both the normal and tangential directions degrades according to the computed hydrogen surface coverage for each element, following the degradation law detailed in Subsection

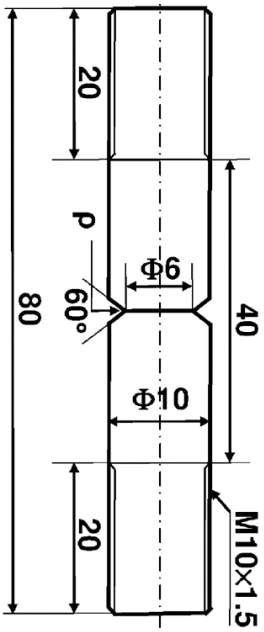

(a) Notched round bar specimen [58]

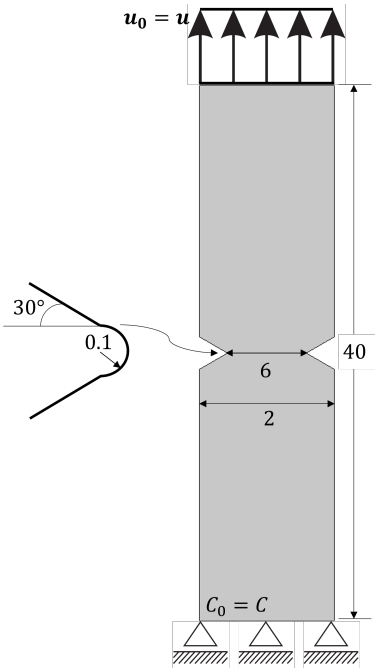

(b) 2D geometry and boundary conditions

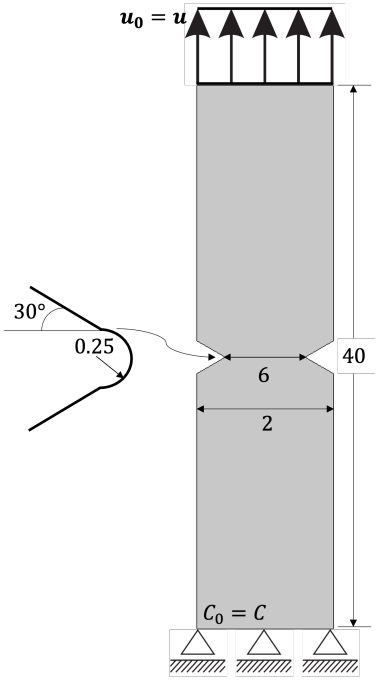

(c) 2D geometry and boundary conditions

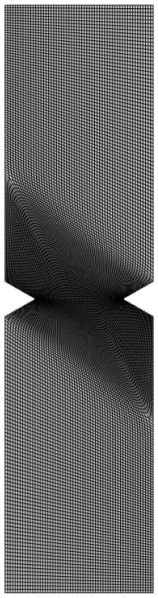

(d) Mesh

Figure 3.6: Schematic representation of the notched cylindrical bar (all dimensions are given in mm)

2.4.1:

$$\begin{aligned} \frac{\sigma_{max}(\theta)}{\sigma_{max}(0)} &= 1 - (1.0467)\theta + (0.1687)\theta^2 \\ \frac{\tau_{max}(\theta)}{\tau_{max}(0)} &= 1 - (1.0467)\theta + (0.1687)\theta^2 \end{aligned} \tag{3.14}$$

Due to hydrogen's tendency to migrate toward regions of high hydrostatic stress, the crack tip becomes a significant attractor, drawing hydrogen from other areas of the material. Figure 3.7 shows a snapshot of the hydrogen concentration just before crack propagation begins for the specimen with $\rho = 0.1$ mm and an initial hydrogen concentration of $C_0 = 0.5$ wt ppm. As illustrated, the hydrogen concentration near the crack tip increases by approximately 30%, compared to the initial hydrogen content, leading to a reduction in material strength as captured by the presented coupled framework.

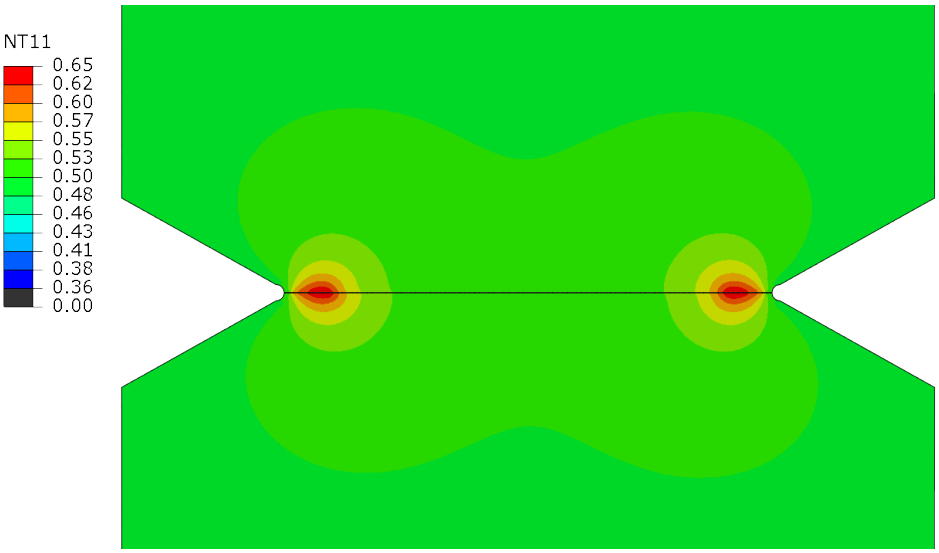

Figure 3.7: Crack tip hydrogen concentration

Figure 3.8 clearly shows a significant reduction in material strength at low hydrogen concentrations. Beyond 1 wt ppm, the decrease in strength reaches saturation. The presented results successfully capture this saturation trend based on the selected degradation law for. However, some discrepancies are observed at the lower hydrogen concentrations at the start of the curve. This may be attributed to the presence of other hydrogen-induced failure mechanisms in the actual experiments, as the current model is limited to simulating only the HEDE mechanism.

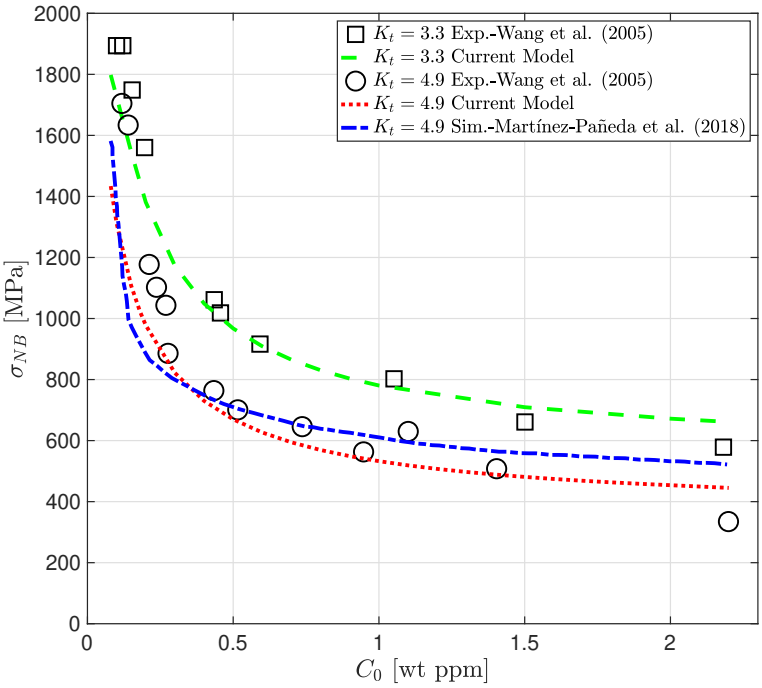

Figure 3.8: Comparison of the obtained numerical results with the experimental results provided in [58] and numerical results provided in [39]

Overall, the presented framework successfully captures the experimental trends for specimens with different notch radii, corresponding to two distinct stress concentration factors. It outperforms the phase field fracture simulation results from the literature, particularly in its accurate prediction of the saturation region of the curve. The results could be further improved by fine-tuning the hydrogen embrittlement law, adjusting the constant parameters in Equation 3.14 to better match the experimental data.

3.3 Polycrystalline RVE Simulations

This section presents the numerical findings from the polycrystalline RVE simulations. As previously mentioned, the RVEs are generated using the Voronoi tessellation algorithm. It should be noted that since the deformation-diffusion-failure coupled framework is implemented for both two-dimensional linear quadrilateral and three-dimensional linear brick elements, the generated microstructures have been meshed

using linear brick elements (C3D8). Consequently, this leads to a zigzag representation of the grain boundaries as can be seen in Figure 3.9, which is less realistic compared to actual grain structures. However, by employing a relatively fine mesh, efforts are made to capture the grain boundaries with sufficient accuracy. There may still be an effect on the intergranular decohesion mechanisms due to the resolved shape of the grain boundaries. However, the mixed-mode cohesive zone framework mitigates this issue. The PPR cohesive zone formulation separately defines the normal and tangential separations using a mixed-mode traction-separation law, allowing for the capture of decohesion in both directions based on the computed traction acting on the cohesive interface elements. This approach allows for the prediction of complex crack paths that propagate not only in the normal direction but also tangentially, effectively reducing the impact of the jagged grain boundary representation.

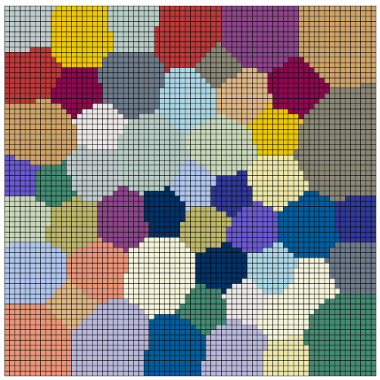

(a) Front meshed view, 50 Grains

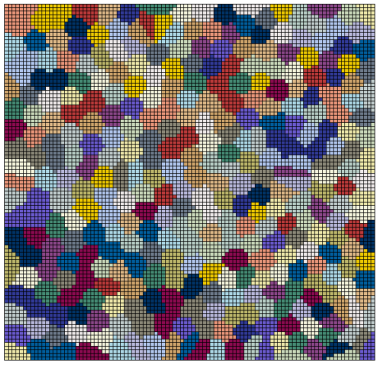

(b) Front meshed view, 350 Grains

Figure 3.9: Mesh used for the 50-grain and 350-grain polycrystals

Two types of microstructures are generated, one with 50 grains and the other with 350 grains. First, simulations are conducted using the local crystal plasticity framework as detailed in Subsection 2.1.1. Subsequently, the simulations are repeated with the strain gradient crystal plasticity model, whose details are given in Subsection 2.1.2 to demonstrate and compare the size effect and nonlocal behavior on the 50-grain polycrystalline RVE. The results are discussed in terms of microstructural and size-dependent effects to provide insights into the micromechanical processes underlying the macroscopic phenomenon of hydrogen embrittlement.

3.3.1 Model and Material Parameters

This subsection outlines the material parameters applied in all the crystal plasticity and strain gradient crystal plasticity simulations, along with the cohesive zone model parameters for intergranular failure and the diffusion-related parameters for the stress-assisted hydrogen transport model.

The crystal plasticity parameters used for the material in this study are adopted from the author's previous work [117] and are summarized in Table 3.1.

Table 3.1: Crystal plasticity material parameters

Slip System	g_s (MPa)	g_0 (MPa)	h_0 (MPa)
$\{112\}\langle 111\rangle$	252	98	475

The cohesive zone model parameters are chosen to effectively capture the microstructural effects on hydrogen-induced failure, particularly by accounting for the critical and final crack widths in both tangential and normal separations. It is important to note that the chosen parameter set is not uniquely tailored to a specific material but is selected to provide results that allow for qualitative discussion of the findings in the presented examples. Selected parameter set is summarized in Table 3.2

Diffusion-related material parameters are taken from the literature [39], and summarized in Table 3.3.

For the polycrystalline RVE simulations, the embrittlement law is chosen to de-

Table 3.2: Cohesive zone model parameters

σ_{max} (MPa)	τ_{max} (MPa)	ϕ_n (N/mm)	ϕ_t (N/mm)	α	β	λ_n	λ_t
300	105	10	10	4.46	2.74	0.01	0.02

Table 3.3: Diffusion-related parameters

D (mm^2/s)	T (K)	$\overline{V}_H$ (mm^3/s)	R (Nmm/molK)
0.0127	300	2000	8314.5

grade the cohesive energy rather than the cohesive strength, as reducing the cohesive strength tends to overestimate crack propagation due to the cohesive model's sensitivity to this parameter. By degrading the cohesive energy instead, the impact of hydrogen content on the results becomes more pronounced.

$$\begin{aligned} \frac{\phi_n(\theta)}{\phi_n(0)} &= 1 - (0.89)\theta \\ \frac{\phi_t(\theta)}{\phi_t(0)} &= 1 - (0.89)\theta \end{aligned} \tag{3.15}$$

3.3.2 50 Grain Polycrystalline RVE Simulations

50-grain polycrystalline RVE, as shown in Figure 3.10 with 10368 bulk C3D8T and 1984 cohesive COH3D8 elements, is generated and simulated using two approaches: first, employing the local crystal plasticity constitutive model, and second, utilizing the nonlocal strain gradient crystal plasticity framework. Both methods are coupled with the stress-driven hydrogen diffusion problem and intergranular failure mechanism. Simulations are first performed without hydrogen, followed by two precharged hydrogen concentration values of $C_0 = 0.5$ wt ppm and $C_0 = 1.0$ wt ppm. These values are defined as initial conditions in ABAQUS, assuming a homogeneous hydrogen distribution within the microscopic specimens. To replicate typical experimental conditions, where tests are often conducted in an aqueous solution with ambient hydrogen concentration matching the precharged value, a boundary condition is applied to the outer nodes, setting the hydrogen concentration equal to the respective initial condition.

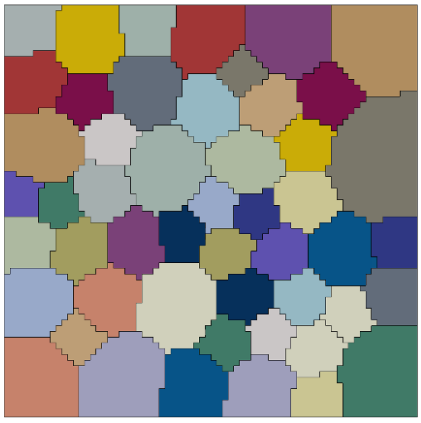

(a) Front view, 50-Grain RVE

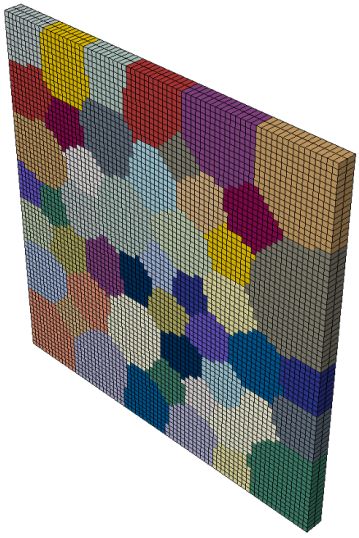

(b) Isometric view with mesh, 50-Grain RVE

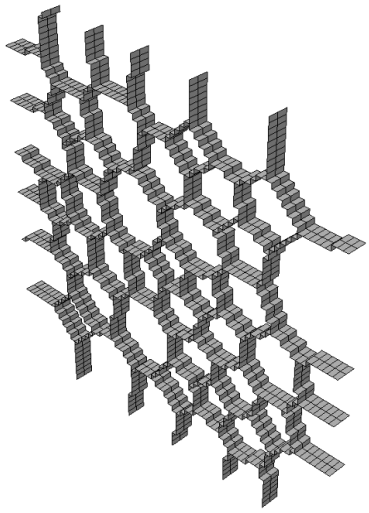

(c) Inserted cohesive zone elements

Figure 3.10: Visualization of 50-Grain RVE

Results from both the local and nonlocal crystal plasticity simulations are presented and compared to gain insights into the microstructural effects under the influence of hydrogen. The boundary conditions, detailed in Subsection 3.1.3, are applied. A relatively long simulation time of $t_{final} = 10^7$ s is chosen to allow hydrogen to diffuse into the fracture process zone during the deformation.

Figure 3.11 presents the true stress—strain curves along with the Von Mises stress contours from the local crystal plasticity simulations for three different initial hydro-

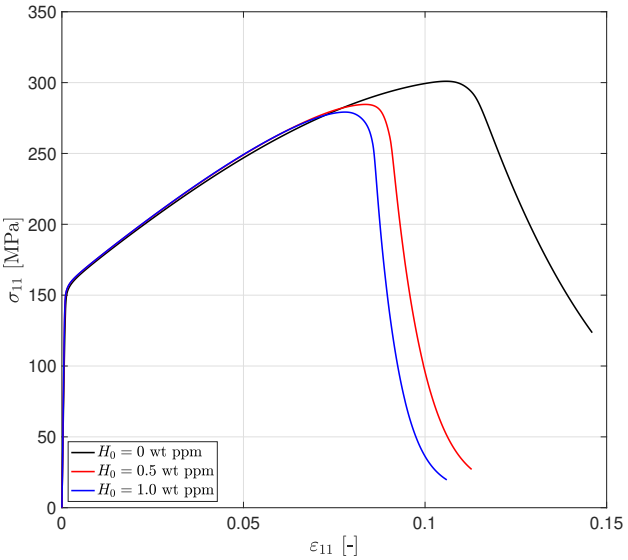

(a) True stress-strain curves

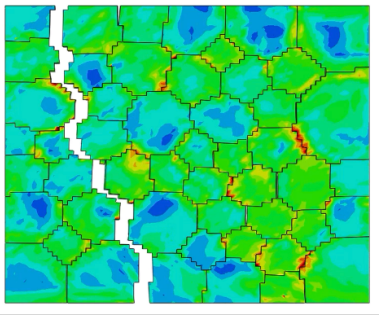

(b) $C_0 = 0$ wt ppm

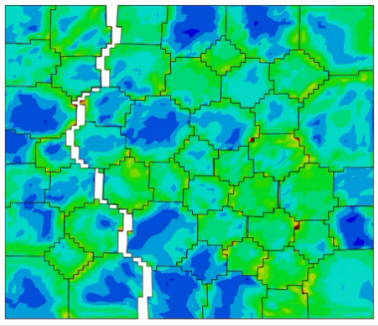

(c) $C_0 = 0.5$ wt ppm

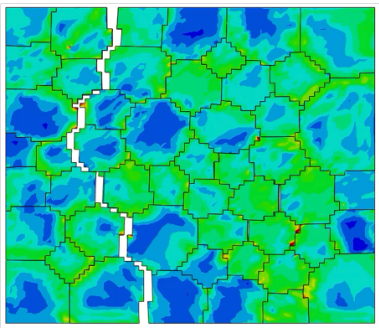

(d) $C_0 = 1.0$ wt ppm

Figure 3.11: True stress-strain curves and Von Mises stress contour plots at the final state of each CPFEM simulation.

gen concentrations. As expected, the introduction of precharged hydrogen significantly weakens the material, resulting in a notable reduction in ultimate stress values. Upon examining the final simulation states with increasing hydrogen content, it is observed that while crack propagation slightly alters in the upper region, crossing two grains, the remainder of the crack path remains largely unaffected. Moreover, in the simulation without hydrogen, no degradation affects intergranular decohesion, allowing stress concentration regions to form along the grain boundaries, away from the propagated crack. However, in the hydrogen-influenced cases, the cohesive energy is reduced, and the material has already undergone a reloading phase, leading to minimal stress concentration due to the onset of micro-separations.

Simulations are subsequently conducted using the strain gradient crystal plasticity constitutive model to examine size effects. A relatively large internal length scale parameter, $l = 1$ mm, is chosen to amplify the influence of size effects and make the differences between the local and nonlocal formulations more pronounced. For details on the internal length scale parameter formulation, please refer to Section 2.1.2. Figure 3.12 presents the true stress-—strain curves along with the Von Mises stress contours from the strain gradient crystal plasticity simulations for three different initial hydrogen concentrations.

The same trend of a significant decrease in ultimate strength is observed here as well. However, with the inclusion of hardening effects due to GNDs, the ultimate stress values for each hydrogen concentration are higher. The primary distinction between the local and nonlocal formulations becomes evident when examining the crack propagation paths in the final deformed state of the material. In the local formulation, apart from a slight variation, the crack propagation path remains largely consistent, even with increasing hydrogen content. In contrast, with the nonlocal formulation, the crack path differs significantly between the no-hydrogen case and the case with a hydrogen concentration of $C_0 = 1.0$ wt ppm.

To assess the influence of the non-local framework, the following contour plots display the results from both crystal plasticity and strain gradient plasticity simulations under identical hydrogen content. Each plot is taken at the ultimate stress point of the respective simulation. Figure 3.13a shows the hydrostatic stress distribution for

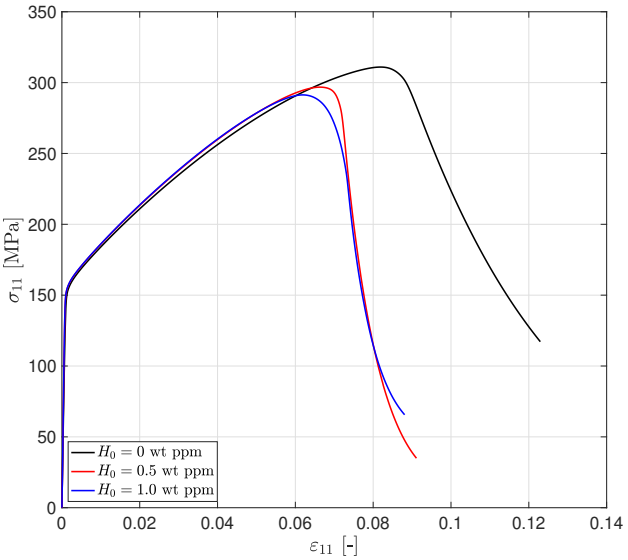

(a) True stress-strain curves

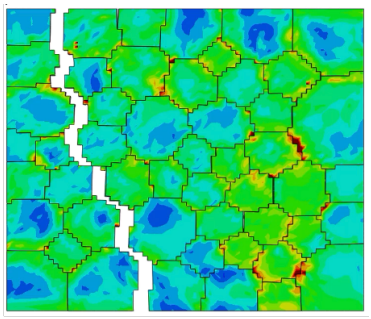

(b) $C_0 = 0$ wt ppm

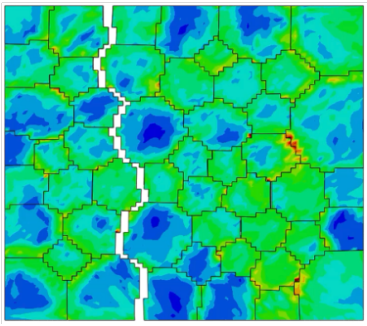

(c) $C_0 = 0.5$ wt ppm

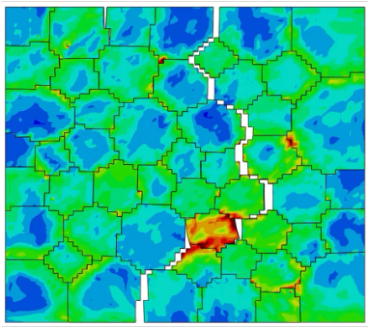

(d) $C_0 = 1.0$ wt ppm

Figure 3.12: True stress-strain curves and Von Mises stress contour plots at the final state of each SGCPFEM simulation with $l = 1$ mm

simulations with $C_0 = 0.5$ wt ppm, comparing the local and non-local approaches. The figure indicates that the introduction of hardening due to GNDs significantly increases the positive hydrostatic stress, particularly along the grain boundaries. This increase in hydrostatic stress promotes greater hydrogen accumulation along the grain boundaries and triple junction points, a phenomenon widely observed and discussed in experimental studies.

Figure 3.13b shows the hydrogen concentration distribution for the $C_0 = 0.5$ wt ppm simulations. As noted earlier, the increase in hydrostatic stress, particularly near grain boundaries and triple junctions, leads to higher hydrogen accumulation in those areas. These findings align with experimental observations, suggesting that strain gradient formulations could enhance the modelling of hydrogen transport in regions prone to higher hydrogen concentrations, as well as improve the prediction of intergranular failure in areas where failure is expected due to the HEDE mechanism.

Figures 3.14a and 3.14b show the hydrostatic stress and hydrogen concentration distributions, respectively, for the $C_0 = 1.0$ wt ppm simulations. Similar trends are observed with the increased level of precharged hydrogen, but this time the rise in hydrostatic stress and concentrated hydrogen around the grain boundaries is even more pronounced. By comparing Figures 3.11d and 3.12d, it is clear that the crack path has significantly altered. This can be explained by the intensified stress concentration effects when utilizing the strain gradient plasticity formulation, especially as the hydrogen content increases. Consequently, the crack path deviates more noticeably. Once verified with experimental data and after determining the strain gradient formulation's material parameters, the nonlocal framework appears to provide more realistic results by capturing the shifts in the crack path as the hydrogen content increases.

For both precharged hydrogen concentration cases, it is important to note that the loading history and the initiation of separations influence the hydrogen concentration distribution and the hydrogen-induced intergranular crack propagation. Simply examining the snapshots at the ultimate stress point does not necessarily indicate that the regions with higher hydrogen concentration will host crack propagation. Other areas may have already experienced higher hydrogen concentration earlier in the loading process, and as cohesive zone elements begin to separate, both the stress (including

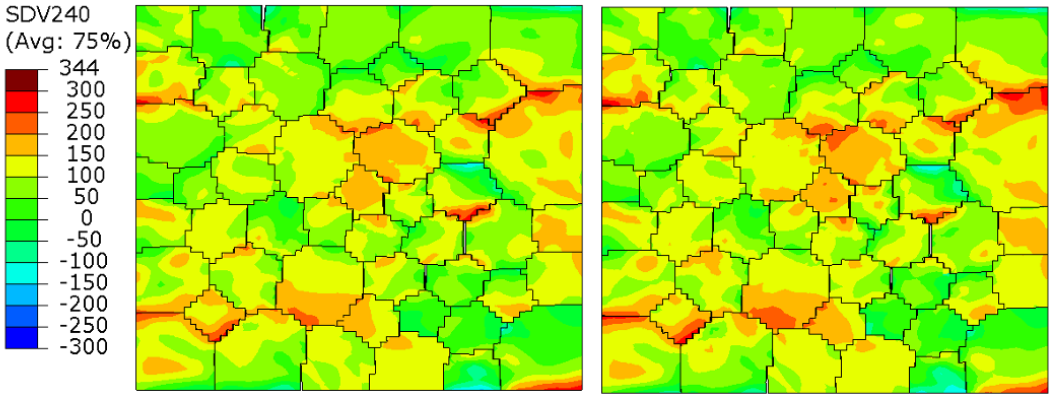

(a) Hydrostatic Stress Distribution

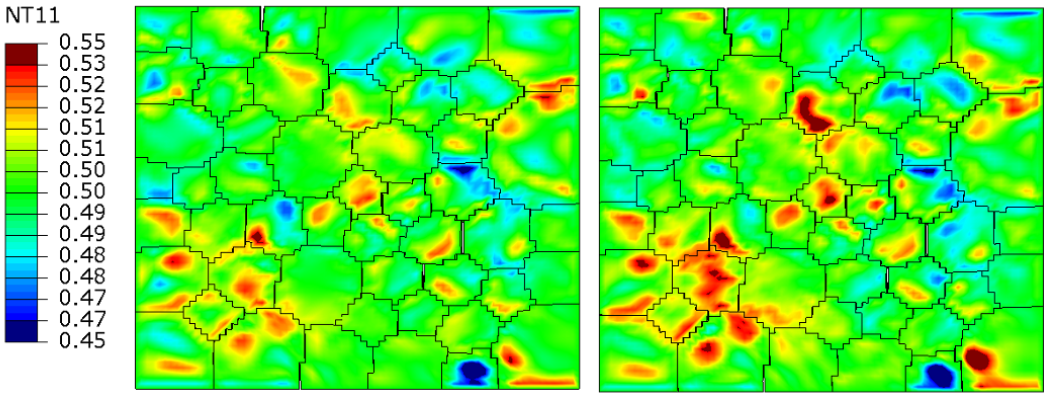

(b) Hydrogen Concentration Distribution

Figure 3.13: Results for precharged hydrogen concentration of $C_0 = 0.5$ wt ppm. Left: CPFEM Results, Right: SGCPFEM Results

hydrostatic stress) and the hydrogen concentration values tend to decrease. These snapshots are selected to qualitatively assess the impact of nonlocal effects, particularly the increased hydrostatic stress and hydrogen concentration near the grain boundaries, and to highlight the potential benefits of incorporating strain gradient formulations.

To discuss the accumulation of GNDs in the nonlocal crystal plasticity formulations, Figure 3.15 is presented. As with the hydrostatic stress and hydrogen concentration contour plots, these snapshots are taken at the point where the stress reaches its ultimate strength in each case. It is evident that the highest accumulation of GNDs occurs in the simulation without hydrogen content, while the effect of GNDs dimin-

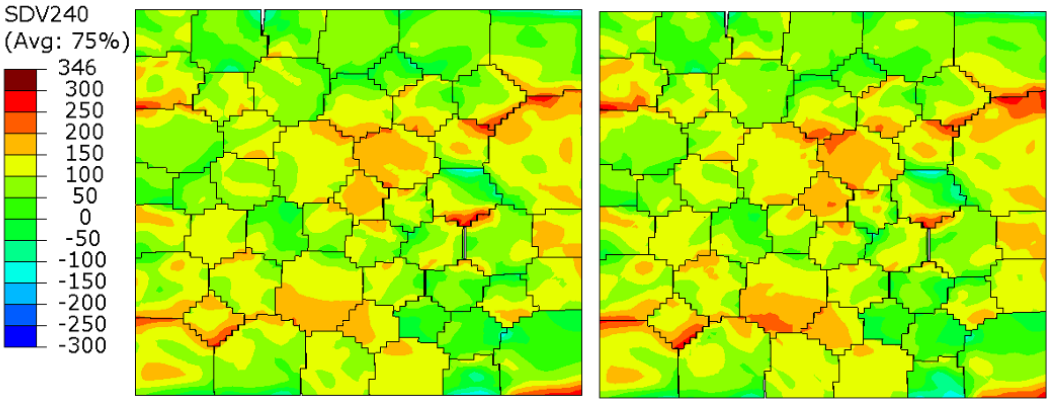

(a) Hydrostatic Stress Distribution

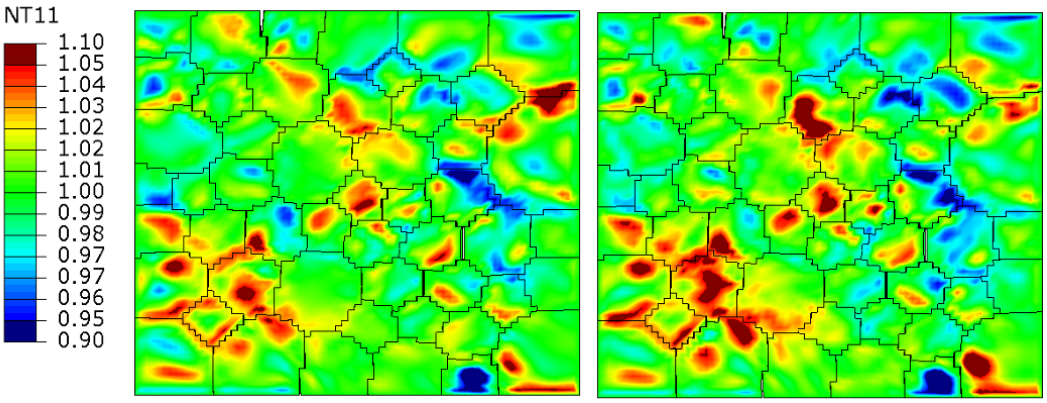

(b) Hydrogen Concentration Distribution

Figure 3.14: Results for precharged hydrogen concentration of $C_0 = 1.0$ wt ppm. Left: CPFEM Results, Right: SGCPFEM Results

ishes as the precharged hydrogen concentration increases. This can be attributed to the competing mechanisms of intergranular decohesion and hardening, particularly around the grain boundaries. As the hydrogen-induced cohesive zone formulation reduces cohesive energy in regions of concentrated hydrostatic stress, decohesion occurs more readily, leading to unloading and a decrease in GND accumulation in those areas. Consequently, as the hydrogen content increases, the GND concentrations decrease.

Lastly, to investigate the grain size effect in the 50-grain RVE simulations, the model is scaled by a factor of 10 by modifying the nodal coordinates, and the simulations are rerun with the constant internal length scale parameter of $l = 1$ mm. Since crystal

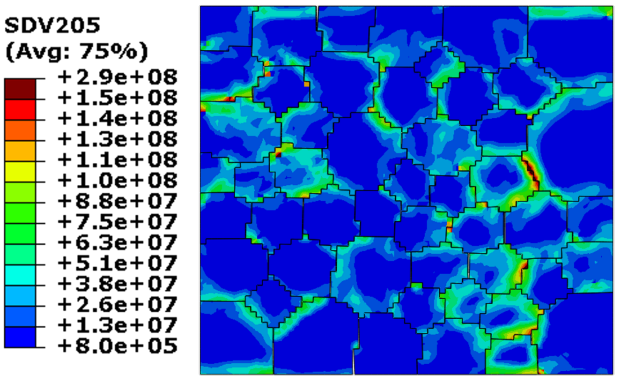

(a) $C_0 = 0$ wt ppm

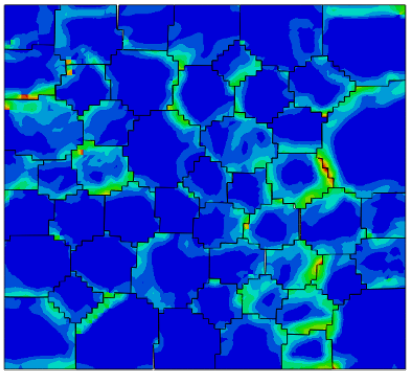

(b) $C_0 = 0.5$ wt ppm

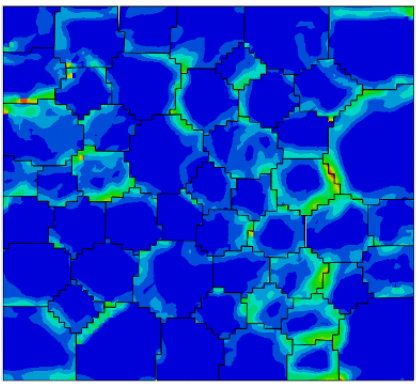

(c) $C_0 = 1.0$ wt ppm

Figure 3.15: Accumulation of GNDs, SGCPFEM simulations with $l = 1$ mm

plasticity is a local framework, simply changing the average grain diameter by scaling the coordinates produces identical results. However, according to the well-known Hall-Petch effect, a material's yield strength increases as grain size decreases, as grain boundaries act as barriers to dislocation movement, making deformation more difficult and thus increasing material strength. Nonlocal plasticity models can capture this phenomenon through the introduction of an internal length scale parameter. In this study, the strain gradient crystal plasticity formulation is applied to assess the impact of grain size changes on hydrogen-induced failure.

Figure 3.16 presents the true stress–strain curves from simulations with two different average grain diameters, 0.124 mm and 1.240 mm, under three precharged hydrogen concentration values: 0, 0.5, and 1.0 wt ppm. As demonstrated, the Hall-Petch effect is evident, with the ultimate strength of the simulations with larger grain diameters

being significantly lower than those with smaller grain diameters.

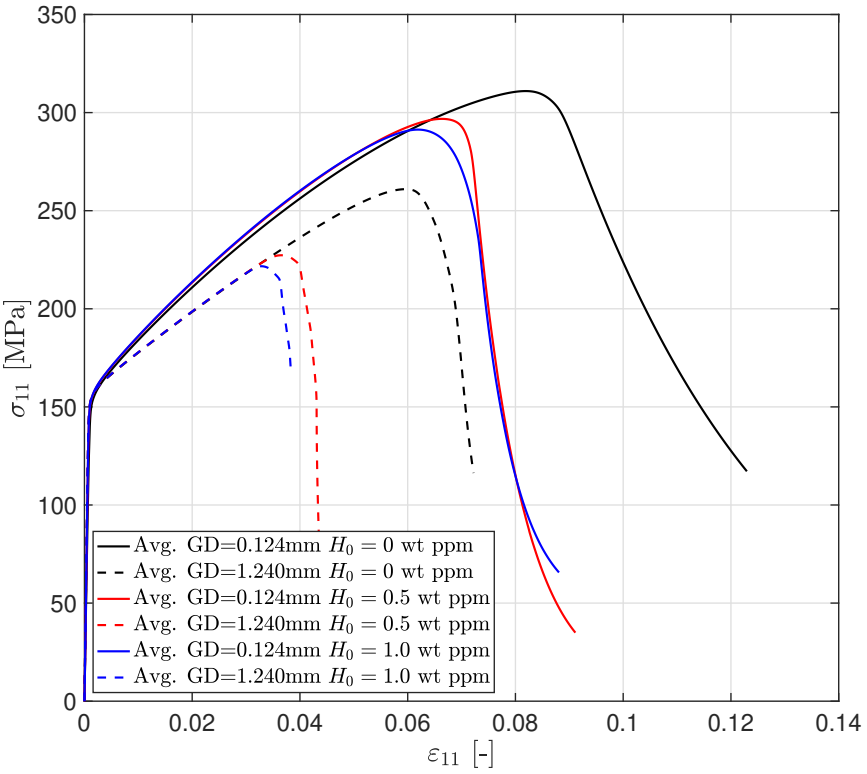

Figure 3.16: Size effect on true stress-strain curves

Figure 3.17 displays the Von Mises stress contours at the final converged state for each simulation, allowing for a comparison of the propagated intergranular crack paths. The variation in average grain size notably impacts the crack propagation paths for each precharged hydrogen concentration, further supporting the use of strain gradient crystal plasticity for micromechanical modelling of hydrogen-induced failure. These findings qualitatively align with literature that emphasizes the influence of grain size on both crack propagation and the shift in the dominant physical failure mechanisms.

Interestingly, as the average grain size increases, the crack propagation path shows little change despite the rise in hydrogen content. In contrast, for smaller grain diameters, the crack propagation pattern shifts significantly with increasing hydrogen concentration. This suggests that while ambient hydrogen does not fundamentally alter the primary intergranular failure mechanism, larger grain sizes cause the microstructure itself to play a more dominant role in governing the failure process.

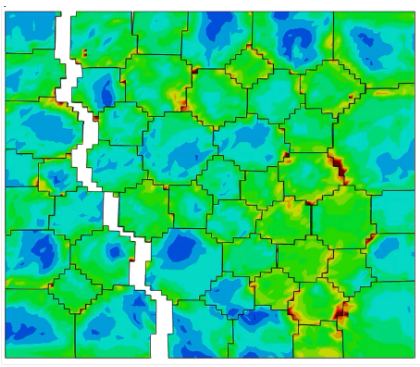

(a) $C_0 = 0$ wt ppm,Avg. GD=0.124 mm

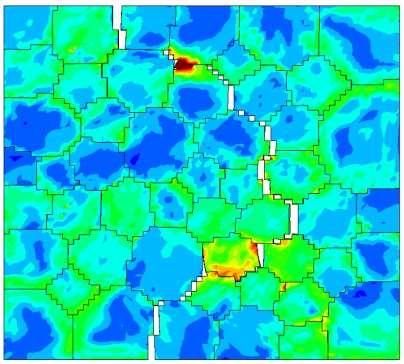

(b) $C_0 = 0$ wt ppm,Avg. GD=1.240 mm

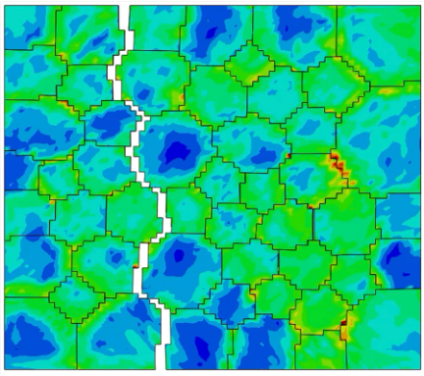

(c) $C_0 = 0.5$ wt ppm,Avg. GD=0.124 mm

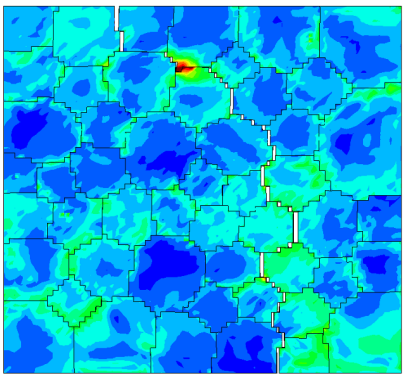

(d) $C_0 = 0.5$ wt ppm,Avg. GD=1.240 mm

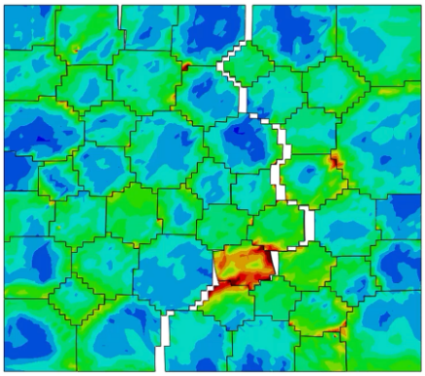

(e) $C_0 = 1.0$ wt ppm,Avg. GD=0.124 mm

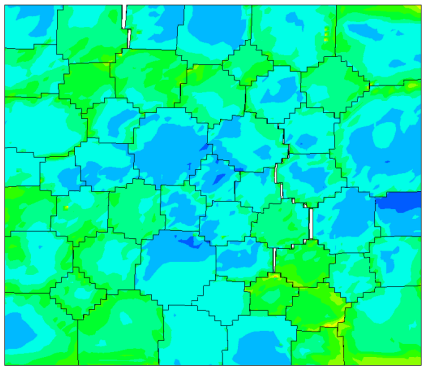

(f) $C_0 = 1.0$ wt ppm, Avg. GD=1.240 mm

Figure 3.17: Comparison of Von Mises stress contour plots at the final state of each SGCPFEM simulation with $l = 1$ mm

Figures 3.18a and 3.18b present the hydrostatic stress and hydrogen concentration contours for a hydrogen content of $C_0 = 0.5$ wt ppm, taken at the ultimate stress point of each simulation. In Figure 3.18a, the simulations with smaller grain sizes clearly

show a higher concentration of hydrostatic stress compared to those with larger grain sizes. This leads to more localized hydrogen concentration in the smaller grain size simulations. These findings suggest that as grain size decreases, the material becomes more susceptible to hydrogen-induced failure, as the localized hydrogen concentrations increase significantly compared to the larger grain size cases.

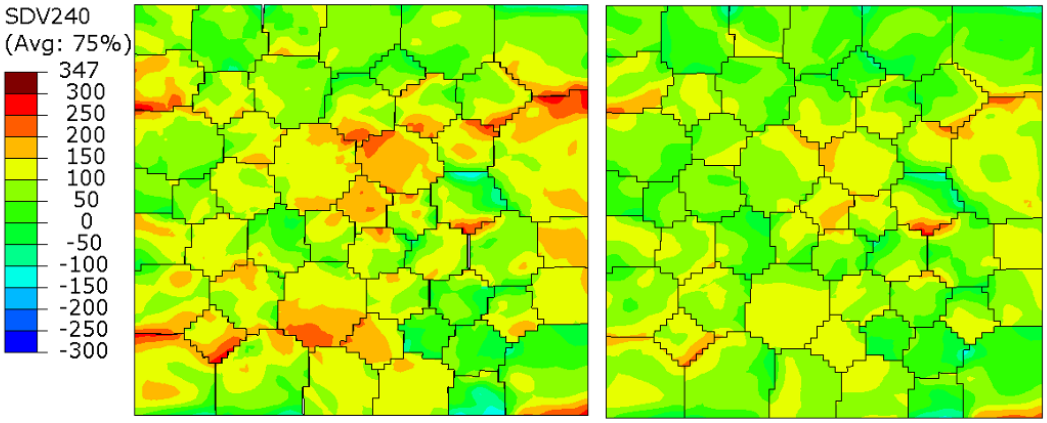

(a) Hydrostatic Stress Distribution

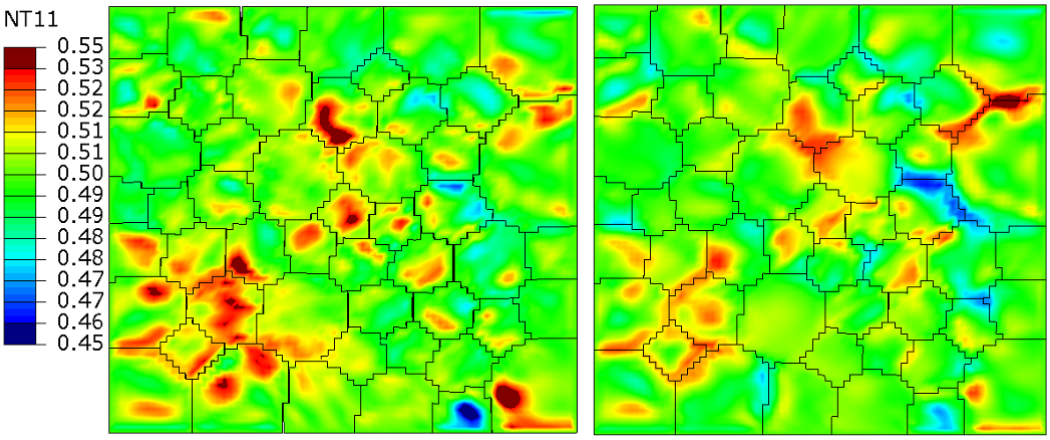

(b) Hydrogen Concentration Distribution

Figure 3.18: Results for precharged hydrogen concentration of $C_0 = 0.5$ wt ppm. Left: Avg. GD=0.124 mm Results, Right: Avg. GD=1.240 mm Results

Similarly, Figures 3.19a and 3.19b display the hydrostatic stress and hydrogen concentration contours for a precharged hydrogen content of $C_0 = 1.0$ wt ppm. The trends observed in the $C_0 = 0.5$ wt ppm simulations persist here as well. However, with the higher hydrogen concentration, the reduction in cohesive energy becomes

more pronounced. In the smaller grain microstructure, the increased localized stress values lead to greater hydrogen accumulation, triggering micro-separations and causing unloading and subsequent dispersion of hydrogen in the regions experiencing decohesion. Consequently, certain areas in the larger grain microstructure exhibit higher local hydrogen concentrations.

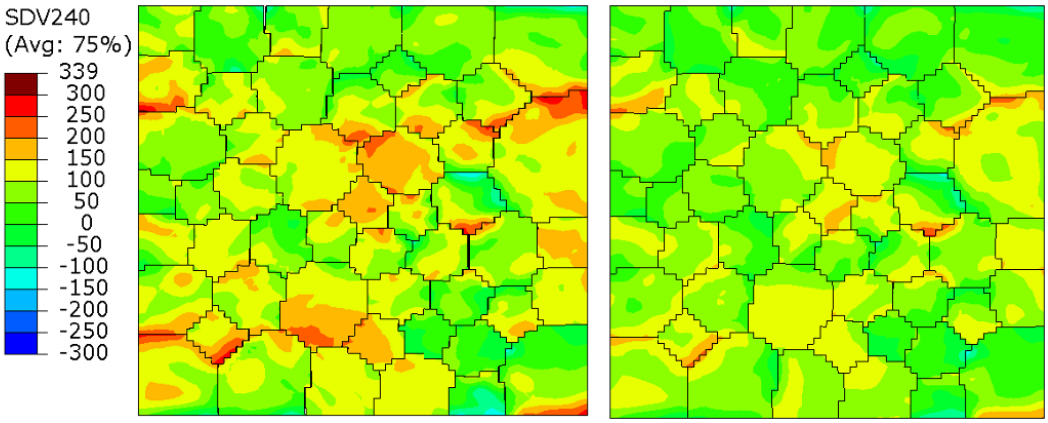

(a) Hydrostatic Stress Distribution

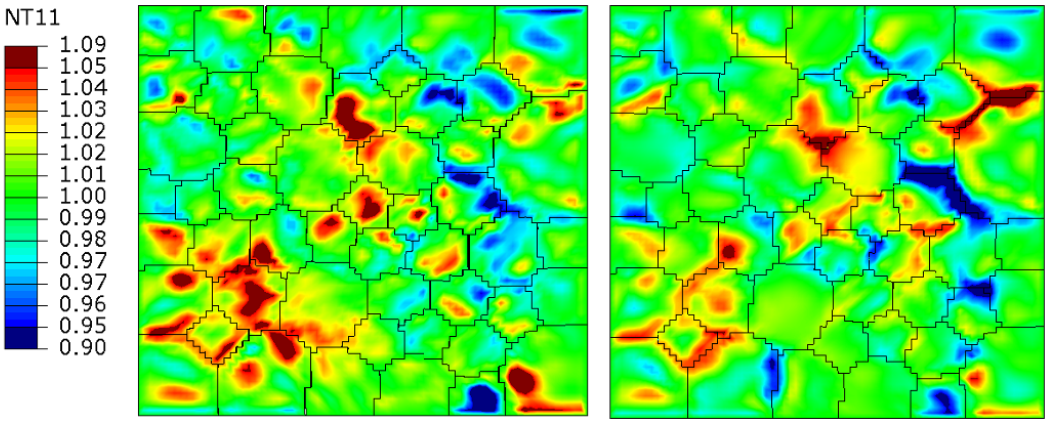

(b) Hydrogen Concentration Distribution

Figure 3.19: Results for precharged hydrogen concentration of $C_0 = 1.0$ wt ppm. Left: Avg. GD=0.124 mm Results, Right: Avg. GD=1.240 mm Results

3.3.3 350 Grain Polycrystalline RVE Simulations

350-grain polycrystalline RVE, as shown in Figure 3.20 with 19602 bulk C3D8T and 8310 cohesive COH3D8 elements, is generated and simulated using two same two

approach as in 50-grain simulations. The primary objective is to assess the influence of grain number on the micromechanical modelling of hydrogen-induced failure. It is important to note that the simulations presented in this section are conducted only at a precharged hydrogen concentration of $C_0 = 0.5$ wt ppm.

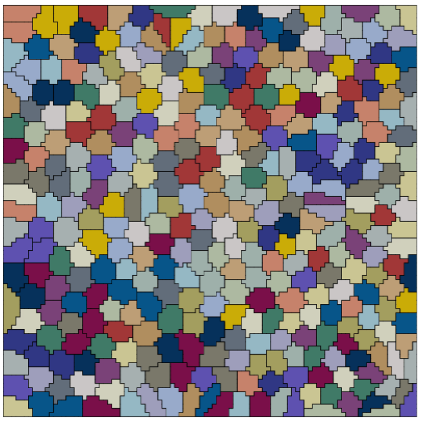

(a) Front view, 350-Grain RVE

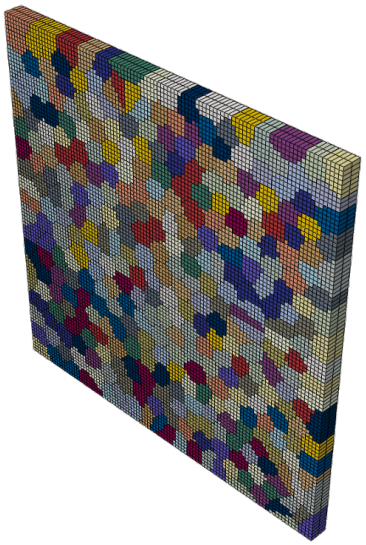

(b) Isometric view with mesh, 350-Grain RVE

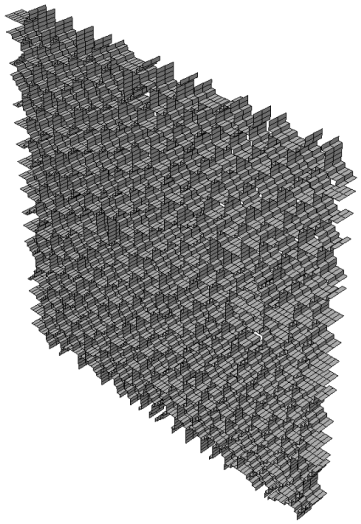

(c) Inserted cohesive zone elements

Figure 3.20: Visualization of 350-Grain RVE

To assess the effect of grain count using both local and nonlocal crystal plasticity formulations, the true stress–strain curves from both approaches are shown in Figure 3.21a. From Figures 3.21b and 3.21c, it is clear that the crack path changes with the introduction of nonlocal effects, underscoring the importance of incorporating

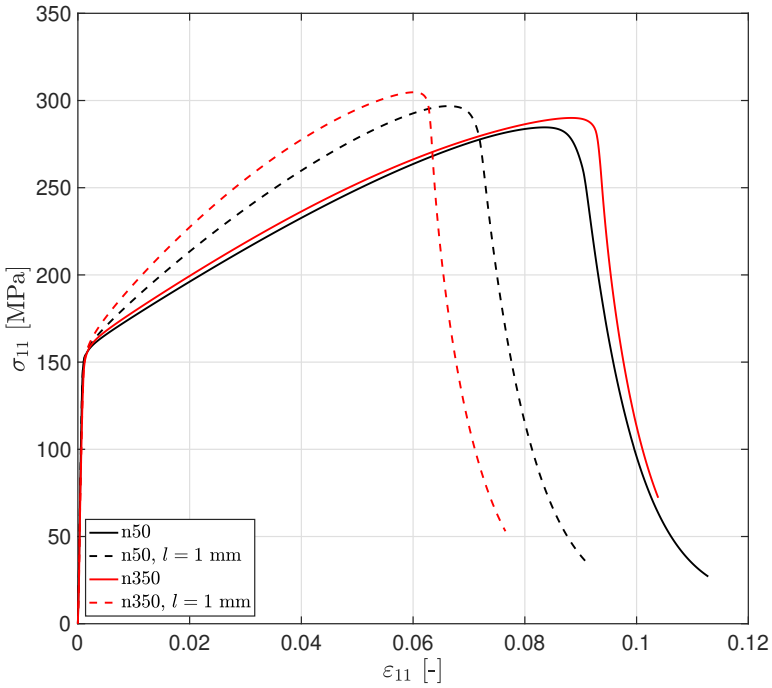

(a) True stress—strain curves for 50 and 350 grain RVEs. Dashed lines represent SGCPFEM simulations with $l = 1$ mm, while solid lines represent CPFEM simulations

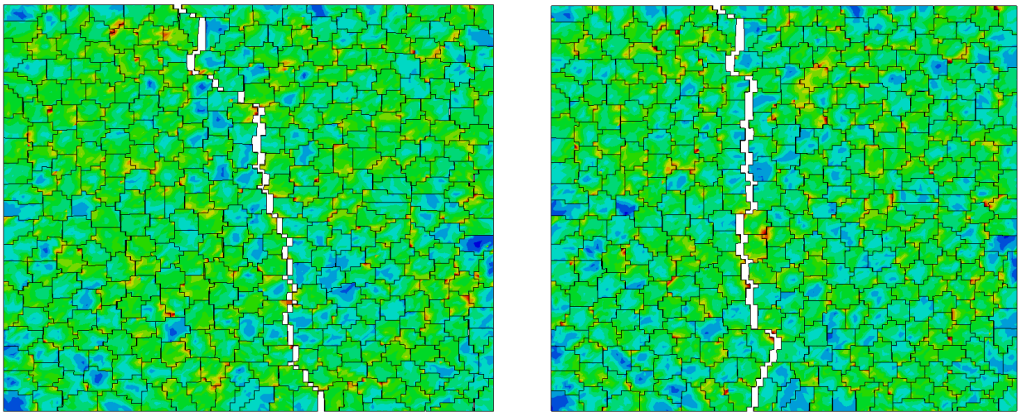

(b) CPFEM simulation

(c) SGCPFEM simulation

Figure 3.21: True stress-strain curves and Von Mises stress contour plots at the final state of each SGCPFEM simulation with $l = 1$ mm

nonlocality into constitutive modelling. The nearly identical flow curves in the local crystal plasticity results of 50 and 350 grain RVE simulations in Figure 3.21a indicate that increasing the number of grains, and thus reducing the average grain size, has no

significant impact on the hardening and failure response in the local framework, as expected. However, with the strain gradient crystal plasticity model, the Hall-Petch effect becomes apparent, as the dashed lines diverge considerably, especially during the hardening phase, indicating a significant size effect.

Figures 3.22b and 3.22c present the distributions of Von Mises stress, hydrostatic stress, and hydrogen concentration at the point of ultimate strength for each simulation. In comparison to the low-grain simulations, the introduction of size effects in the model is less pronounced in the 350-grain simulations, although the observed trends—such as increased stress and hydrogen concentration with strain gradient crystal plasticity—remain consistent. This suggests that when conducting micromechanical modelling of hydrogen-induced failure, it is essential to study and account for the number of grains in the model to ensure that the observed micromechanical effects and trends remain consistent across different grain counts.

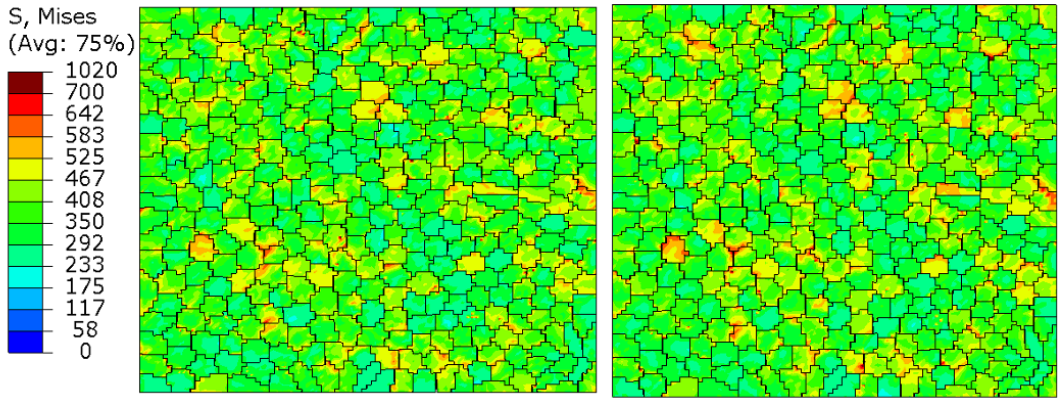

(a) Von Mises Stress Distribution

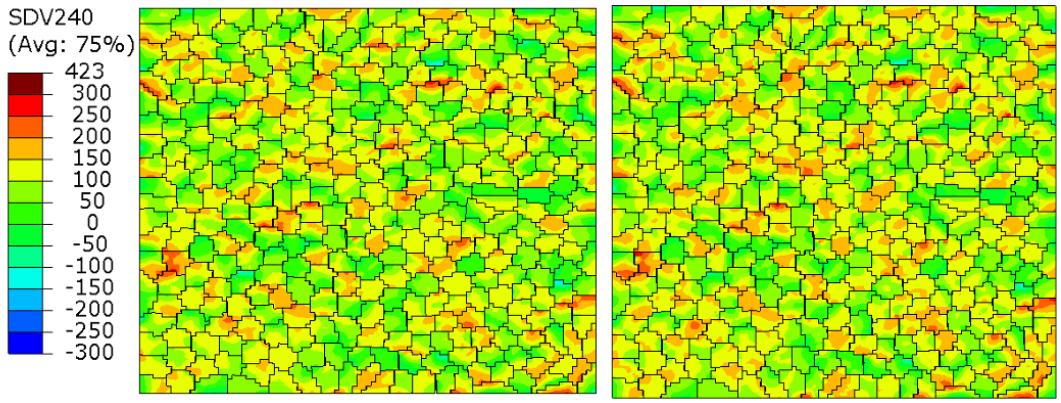

(b) Hydrostatic Stress Distribution

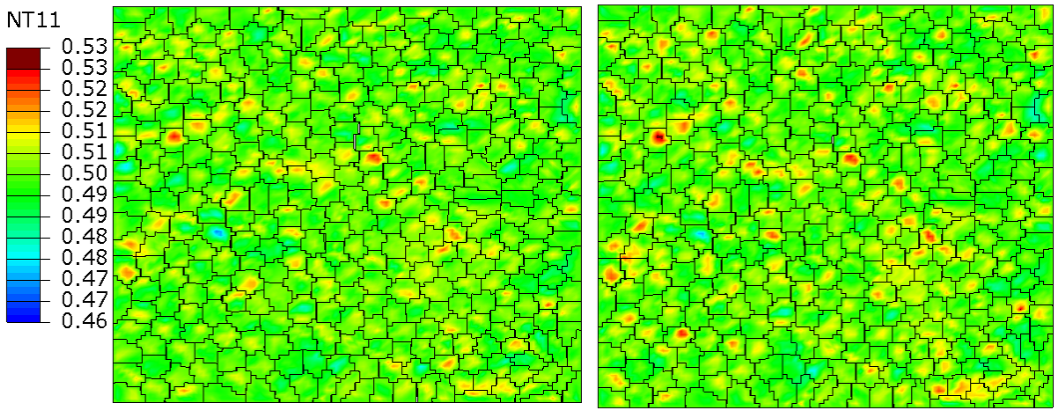

(c) Hydrogen Concentration Distribution

Figure 3.22: Results for precharged hydrogen concentration of $C_0 = 0.5$ wt ppm. Left: CPFEM Results, Right: SGCPFEM Results

CHAPTER 4

CONCLUSIONS

This thesis integrates a potential-based mixed-mode cohesive zone model with a stress-driven hydrogen transport model and implements constitutive laws including von Mises plasticity, crystal plasticity, and strain gradient crystal plasticity within the commercial finite element software ABAQUS.

The coupled framework is applied to both 2D and 3D simulations. While validation is performed using two-dimensional macroscopic notched specimens, the primary findings are derived from three-dimensional polycrystalline microstructure simulations. Polycrystalline microstructures are generated through a Voronoi tessellation algorithm, varying the grain size and number of grains. Extensive preprocessing is conducted using several in-house scripts on the input files for polycrystalline structures. First, the grain boundary interfaces are identified to insert cohesive zone elements. Next, contact surfaces are defined to enable hydrogen transport between neighboring grains, bypassing the cohesive zone elements at the interfaces.

The effect of microstructure on the material's homogenized macroscopic response is assessed by comparing the results from crystal plasticity finite element simulations. This comparison includes both macroscopic stress-strain curves and microscopic insights, such as regions of hydrogen accumulation and areas of localized stress and strain concentrations.

Following this, strain gradient crystal plasticity simulations are performed to investigate the nonlocal effects on the failure of polycrystalline structures influenced by hydrogen. As emphasized in the literature, GNDs have a significant impact on stress concentration regions, particularly around the crack tip, a finding that is further val-

idated by the numerical results presented in this thesis. Incorporating strain gradient effects into the crystal plasticity model is shown to significantly increase stress concentrations at grain boundaries, crack tips, and fracture process zones. This, in turn, results in higher hydrogen concentrations in these regions, strongly affecting the failure mechanism by even altering the crack paths.

The study also examines the grain size effect, showing that, due to the well-known Hall-Petch effect, smaller-sized grain specimens are more prone to hydrogen accumulation near grain boundaries and triple junction points. This is driven by increased localized stress and strain, suggesting that nonlocal plasticity formulations, which can capture size effects, are crucial for micromechanical modeling of hydrogen-induced failure.

Overall, the proposed framework for modeling the hydrogen-enhanced decohesion mechanism through intergranular failure, using a hydrogen-informed cohesive zone model, shows strong potential based on qualitative comparisons with findings from the literature. While further validation against micromechanical experiments is necessary, the results are promising and indicate that the framework effectively captures key features involved in hydrogen-induced failure. Future work should focus on incorporating more realistic microstructures, extending the coupled formulation to tetrahedral finite elements for improved microstructural accuracy, and further exploring the effects of hydrogen degradation laws. Additionally, incorporating hydrogen-sensitive constitutive laws to account for hydrogen's effect on plasticity, and thus attempting to model the combined impact of hydrogen-enhanced localized plasticity failure mechanisms alongside the studied hydrogen-enhanced decohesion mechanism on micromechanical modeling, is a crucial direction for future research.

REFERENCES

[1] O. Barrera, D. Bombac, Y. Chen, T. D. Daff, E. Galindo-Nava, P. Gong, D. Haley, R. Horton, I. Katzarov, J. R. Kermode, C. Liverani, M. Stopher, and F. Sweeney, "Understanding and mitigating hydrogen embrittlement of steels: a review of experimental, modelling and design progress from atomistic to continuum," *Journal of Materials Science*, vol. 53, no. 9, pp. 6251–6290, 2018.

[2] T. Neeraj, R. Srinivasan, and J. Li, "Hydrogen embrittlement of ferritic steels: Observations on deformation microstructure, nanoscale dimples and failure by nanovoiding," *Acta Materialia*, vol. 60, no. 13-14, pp. 5160–5171, 2012.

[3] X. Li, J. Zhang, Q. Fu, X. Song, S. Shen, and Q. Li, "A comparative study of hydrogen embrittlement of 20SiMn2CrNiMo, PSB1080 and PH13-8Mo high strength steels," *Materials Science and Engineering: A*, vol. 724, pp. 518–528, 2018.

[4] E. V. Chatzidouros, A. Traidia, R. S. Devarapalli, D. I. Pantelis, T. A. Steriotis, and M. Jouiad, "Effect of hydrogen on fracture toughness properties of a pipeline steel under simulated sour service conditions," *International Journal of Hydrogen Energy*, vol. 43, no. 11, pp. 5747–5759, 2018.

[5] S. Pallaspuro, H. Yu, A. Kisko, D. Porter, and Z. Zhang, "Fracture toughness of hydrogen charged as-quenched ultra-high-strength steels at low temperatures," *Materials Science and Engineering: A*, vol. 688, pp. 190–201, 2017.

[6] R. Wang, "Effects of hydrogen on the fracture toughness of a X70 pipeline steel," *Corrosion Science*, vol. 51, no. 12, pp. 2803–2810, 2009.

[7] J. A. Ronevich, B. P. Somerday, and C. W. San Marchi, "Effects of microstructure banding on hydrogen assisted fatigue crack growth in X65 pipeline steels," *International Journal of Fatigue*, vol. 82, pp. 497–504, 2016.

[8] A. Alvaro, D. Wan, V. Olden, and A. Barnoush, "Hydrogen enhanced fatigue

crack growth rates in a ferritic Fe-3 wt%Si alloy and a X70 pipeline steel," *Engineering Fracture Mechanics*, vol. 219, p. 106641, 2019.

[9] T. Zhao, Z. Liu, X. Xu, Y. Li, C. Du, and X. Liu, "Interaction between hydrogen and cyclic stress and its role in fatigue damage mechanism," *Corrosion Science*, vol. 157, pp. 146–156, 2019.

[10] J. Venezuela, Q. Liu, M. Zhang, Q. Zhou, and A. Atrens, "The influence of hydrogen on the mechanical and fracture properties of some martensitic advanced high strength steels studied using the linearly increasing stress test," *Corrosion Science*, vol. 99, pp. 98–117, 2015.

[11] Q. Liu, Q. Zhou, J. Venezuela, M. Zhang, J. Wang, and A. Atrens, "A review of the influence of hydrogen on the mechanical properties of DP, TRIP, and TWIP advanced high-strength steels for auto construction," *Corrosion Reviews*, vol. 34, no. 3, pp. 127–152, 2016.

[12] Q. Liu, Q. Zhou, J. Venezuela, M. Zhang, and A. Atrens, "Hydrogen influence on some advanced high-strength steels," *Corrosion Science*, vol. 125, pp. 114–138, 2017.

[13] S. K. Dwivedi and M. Vishwakarma, "Hydrogen embrittlement in different materials: A review," *International Journal of Hydrogen Energy*, vol. 43, no. 46, pp. 21603–21616, 2018.

[14] I. M. Robertson, P. Sofronis, A. Nagao, M. L. Martin, S. Wang, D. W. Gross, and K. E. Nygren, "Hydrogen Embrittlement Understood," *Metallurgical and Materials Transactions A: Physical Metallurgy and Materials Science*, vol. 46, no. 6, pp. 2323–2341, 2015.

[15] W. H. Johnson, "On some remarkable changes produced in iron and steel by the action of hydrogen and acids," *Nature*, vol. 11, no. 281, p. 393, 1875.

[16] M. B. Djukic, G. M. Bakic, V. Sijacki Zeravcic, A. Sedmak, and B. Rajicic, "The synergistic action and interplay of hydrogen embrittlement mechanisms in steels and iron: Localized plasticity and decohesion," *Engineering Fracture Mechanics*, vol. 216, no. February, p. 106528, 2019.

[17] L. B. Pfeil and H. C. H. Carpenter, “The effect of occluded hydrogen on the tensile strength of iron,” *Proceedings of the Royal Society of London. Series A, Containing Papers of a Mathematical and Physical Character*, vol. 112, no. 760, pp. 182–195, 1926.

[18] M. L. Martin, B. P. Somerday, R. O. Ritchie, P. Sofronis, and I. M. Robertson, “Hydrogen-induced intergranular failure in nickel revisited,” *Acta Materialia*, vol. 60, no. 6-7, pp. 2739–2745, 2012.

[19] H. Gao, W. Cao, C. Fang, and E. R. de los Rios, “Analysis of crack tip hydrogen distribution under i/ii mixed mode loads,” *Fatigue & Fracture of Engineering Materials & Structures*, vol. 17, no. 10, pp. 1213–1220, 1994.

[20] J. Lufrano and P. Sofronis, “Enhanced hydrogen concentrations ahead of rounded notches and cracks—competition between plastic strain and hydrostatic stress,” *Acta Materialia*, vol. 46, no. 5, pp. 1519–1526, 1998.

[21] C. D. Beachem, “A new model for hydrogen-assisted cracking (hydrogen "embrittlement"),” *Metallurgical Transactions*, vol. 3, no. 2, pp. 441–455, 1972.

[22] M. Kappes, M. Iannuzzi, and R. M. Carranza, “Hydrogen Embrittlement of Magnesium and Magnesium Alloys: A Review,” *Journal of The Electrochemical Society*, vol. 160, no. 4, pp. C168–C178, 2013.

[23] I. M. Robertson, “The effect of hydrogen on dislocation dynamics,” *Engineering Fracture Mechanics*, vol. 68, no. 6, pp. 671–692, 2001.

[24] X. Li, J. Zhang, E. Akiyama, Q. Fu, and Q. Li, “Hydrogen embrittlement behavior of Inconel 718 alloy at room temperature,” *Journal of Materials Science & Technology*, vol. 35, no. 4, pp. 499–502, 2019.

[25] D. Xie, S. Li, M. Li, Z. Wang, P. Gumbsch, J. Sun, E. Ma, J. Li, and Z. Shan, “Hydrogenated vacancies lock dislocations in aluminium,” *Nature Communications*, vol. 7, pp. 1–7, 2016.

[26] M. Nagumo, “Hydrogen related failure of steels – a new aspect,” *Materials Science and Technology*, vol. 20, no. 8, pp. 940–950, 2004.

[27] K. Sakaki, T. Kawase, M. Hirato, M. Mizuno, H. Araki, Y. Shirai, and M. Nagumo, "The effect of hydrogen on vacancy generation in iron by plastic deformation," *Scripta Materialia*, vol. 55, no. 11, pp. 1031–1034, 2006.

[28] M. Wen, L. Zhang, B. An, S. Fukuyama, and K. Yokogawa, "Hydrogen-enhanced dislocation activity and vacancy formation during nanoindentation of nickel," *Physical Review B - Condensed Matter and Materials Physics*, vol. 80, no. 9, p. 94113, 2009.

[29] C. D. Cann and E. E. Sexton, "Electron Optical Study of Hydride Precipitation and Growth At Crack Tips in Zirconium," *Acta Metallurgica*, vol. 28, no. 9, pp. 1215–1221, 1980.

[30] R. Dutton, K. Nuttall, M. P. Puls, and L. A. Simpson, "Mechanisms of hydrogen induced delayed cracking in hydride forming materials," *Metallurgical Transactions A*, vol. 8 A, no. 10, pp. 1553–1562, 1977.

[31] S. Wang, M. L. Martin, P. Sofronis, S. Ohnuki, N. Hashimoto, and I. M. Robertson, "Hydrogen-induced intergranular failure of iron," *Acta Materialia*, vol. 69, pp. 275–282, 2014.

[32] M. B. Djukic, V. Sijacki Zeravcic, G. M. Bakic, A. Sedmak, and B. Rajicic, "Hydrogen damage of steels: A case study and hydrogen embrittlement model," *Engineering Failure Analysis*, vol. 58, pp. 485–498, 2015.

[33] X. Li, X. Ma, J. Zhang, E. Akiyama, Y. Wang, and X. Song, "Review of Hydrogen Embrittlement in Metals: Hydrogen Diffusion, Hydrogen Characterization, Hydrogen Embrittlement Mechanism and Prevention," *Acta Metallurgica Sinica (English Letters)*, vol. 33, no. 6, pp. 759–773, 2020.

[34] S. P. Lynch, "Progress towards understanding mechanisms of hydrogen embrittlement and stress corrosion cracking," 2007.

[35] J. Song and W. A. Curtin, "Atomic mechanism and prediction of hydrogen embrittlement in iron," *Nature Materials*, vol. 12, no. 2, pp. 145–151, 2013.

[36] X. Xing, J. Gou, F. Li, Y. Zhang, J. Cheng, Y. Wang, J. Liu, G. Cui, Z. Li, P. Zhang, X. Luo, and B. Wang, "Hydrogen effect on the intergranular fail-

ure in polycrystal α-iron with different crystal sizes," *International Journal of Hydrogen Energy*, vol. 46, no. 73, pp. 36528–36538, 2021.

[37] W. Barrows, R. Dingreville, and D. Spearot, "Traction-separation relationships for hydrogen induced grain boundary embrittlement in nickel via molecular dynamics simulations," *Materials Science and Engineering: A*, vol. 650, pp. 354–364, 2016.

[38] B. Tatli, C. Erdoğan, M. E. Özcan, and T. Yalçinkaya, "Phase field fracture modelling of crack initiation and propagation in dual-phase microstructures," *Procedia Structural Integrity*, vol. 61, pp. 12–19, 2024. 3rd International Workshop on Plasticity, Damage and Fracture of Engineering Materials (IW-PDF 2023).

[39] E. Martínez-Pañeda, A. Golahmar, and C. F. Niordson, "A phase field formulation for hydrogen assisted cracking," *Computer Methods in Applied Mechanics and Engineering*, vol. 342, pp. 742–761, 2018.

[40] C. Huang and X. Gao, "Phase field modeling of hydrogen embrittlement," *International Journal of Hydrogen Energy*, vol. 45, no. 38, pp. 20053–20068, 2020.

[41] J. Zhao and Y. F. Cheng, "A phase field method for predicting hydrogen-induced cracking on pipelines," *International Journal of Mechanical Sciences*, vol. 283, p. 109651, 2024.

[42] T. P. Hage, "Application of a coupled diffusion-deformation phase field fracture model for simulations of hydrogen-assisted cracking in x65 steel," Master's thesis, NTNU, 2024.

[43] S. Waseem, C. Erdogan, and T. Yalçinkaya, "Phase field modeling of fatigue crack growth retardation under single cycle overloads," *International Journal of Fatigue*, vol. 179, p. 108064, 2024.

[44] O. Bulut, C. Erdogan, and T. Yalçinkaya, "Dwell fatigue fracture in ti microstructures through crystal plasticity and phase field fracture frameworks," *Procedia Structural Integrity*, vol. 61, pp. 3–11, 2024. 3rd International Work-

shop on Plasticity, Damage and Fracture of Engineering Materials (IWPDF 2023).

[45] S. Waseem, İzzet Erkin Ünsal, and T. Yalçinkaya, "Phase field modelling of fatigue crack growth at constant and variable amplitude loading," *Procedia Structural Integrity*, vol. 42, pp. 1692–1699, 2022. 23 European Conference on Fracture.

[46] A. Golahmar, P. K. Kristensen, C. F. Niordson, and E. Martínez-Pañeda, "A phase field model for hydrogen-assisted fatigue," *International Journal of Fatigue*, vol. 154, p. 106521, 2022.

[47] C. Cui, P. Bortot, M. Ortolani, and E. Martínez-Pañeda, "Computational predictions of hydrogen-assisted fatigue crack growth," *International Journal of Hydrogen Energy*, vol. 72, pp. 315–325, 2024.

[48] Y. Z. Wang, J. Z. Zhang, L. Yang, and X. L. Du, "A phase field framework for corrosion fatigue of carbon steel," *International Journal of Fatigue*, vol. 190, p. 108603, 2025.

[49] M. Lin, H. Yu, X. Wang, R. Wang, Y. Ding, A. Alvaro, V. Olden, J. He, and Z. Zhang, "A microstructure informed and mixed-mode cohesive zone approach to simulating hydrogen embrittlement," *International Journal of Hydrogen Energy*, vol. 47, no. 39, pp. 17479–17493, 2022.

[50] I. Tandogan and T. Yalcinkaya, "Development and implementation of a micromechanically motivated cohesive zone model for ductile fracture," *International Journal of Plasticity*, vol. 158, p. 103427, 2022.

[51] T. Yalçinkaya and A. Cocks, "Micromechanical cohesive zone relations for ductile fracture," *Procedia Structural Integrity*, vol. 2, pp. 1716–1723, 2016. 21st European Conference on Fracture, ECF21, 20-24 June 2016, Catania, Italy.

[52] T. Yalçinkaya, I. T. Tandogan, and A. Cocks, "Development of a micromechanics based cohesive zone model and application for ductile fracture," *Procedia Structural Integrity*, vol. 21, pp. 52–60, 2019. 1st International Workshop on

Plasticity, Damage and Fracture of Engineering Materials, IWPDF 2019, 22-23 August 2019, Ankara, Turkey.

[53] C. Moriconi, G. Hénaff, and D. Halm, "Cohesive zone modeling of fatigue crack propagation assisted by gaseous hydrogen in metals," *International Journal of Fatigue*, vol. 68, pp. 56–66, 2014.

[54] R. Falkenberg, W. Brocks, W. Dietzel, and I. Scheider, "Modelling the effect of hydrogen on ductile tearing resistance of steels," *International Journal of Materials Research*, vol. 101, no. 8, pp. 989–996, 2010.

[55] W. Brocks, R. Falkenberg, and I. Scheider, "Coupling aspects in the simulation of hydrogen-induced stresscorrosion cracking," *Procedia IUTAM*, vol. 3, pp. 11–24, 2012.

[56] A. Alvaro, V. Olden, and O. M. Akselsen, "3D cohesive modelling of hydrogen embrittlement in the heat affected zone of an X70 pipeline steel – Part II," *International Journal of Hydrogen Energy*, vol. 39, no. 7, pp. 3528–3541, 2014.

[57] O. Barrera and A. C. Cocks, "Computational modelling of hydrogen embrittlement in welded structures," *Philosophical Magazine*, vol. 93, no. 20, pp. 2680–2700, 2013.

[58] M. Wang, E. Akiyama, and K. Tsuzaki, "Effect of hydrogen and stress concentration on the notch tensile strength of AISI 4135 steel," *Materials Science and Engineering: A*, vol. 398, no. 1-2, pp. 37–46, 2005.

[59] B. Sobhaniaragh, S. H. Afzalimir, and C. Ruggieri, "Towards the prediction of hydrogen–induced crack growth in high–graded strength steels," *Thin-Walled Structures*, vol. 159, no. May 2020, 2021.

[60] H. Yu, J. S. Olsen, V. Olden, A. Alvaro, J. He, and Z. Zhang, "Cohesive zone simulation of grain size and misorientation effects on hydrogen embrittlement in nickel," *Engineering Failure Analysis*, vol. 81, pp. 79–93, 2017.

[61] T. Yalçinkaya, İzzet Özdemir, and İzzet Tarik Tandoğan, "Misorientation and grain boundary orientation dependent grain boundary response in polycrys-

talline plasticity," *Computational Mechanics*, vol. 67, no. 3, pp. 937–954, 2021.

[62] A. Valverde-González, E. Martínez-Pañeda, A. Quintanas-Corominas, J. Reinoso, and M. Paggi, "Computational modelling of hydrogen assisted fracture in polycrystalline materials," *International Journal of Hydrogen Energy*, vol. 47, no. 75, pp. 32235–32251, 2022.

[63] J. Y. Wu, T. K. Mandal, and V. P. Nguyen, "A phase-field regularized cohesive zone model for hydrogen assisted cracking," *Computer Methods in Applied Mechanics and Engineering*, vol. 358, p. 112614, 2020.

[64] J. Y. Wu, "A unified phase-field theory for the mechanics of damage and quasi-brittle failure," *Journal of the Mechanics and Physics of Solids*, vol. 103, pp. 72–99, 2017.

[65] T. K. Mandal, V. P. Nguyen, and J. Y. Wu, "Comparative study of phase-field damage models for hydrogen assisted cracking," *Theoretical and Applied Fracture Mechanics*, vol. 111, p. 102840, 2021.

[66] S. Zhang and Q. Shen, "A Phase-Field Regularized Cohesion Model for Hydrogen-Assisted Cracking," *Coatings*, vol. 14, no. 2, p. 202, 2024.

[67] A. Baktheer, E. Martínez-Pañeda, and F. Aldakheel, "Phase field cohesive zone modeling for fatigue crack propagation in quasi-brittle materials," *Computer Methods in Applied Mechanics and Engineering*, vol. 422, p. 116834, 2024.

[68] S. del Busto, C. Betegón, and E. Martínez-Pañeda, "A cohesive zone framework for environmentally assisted fatigue," *Engineering Fracture Mechanics*, vol. 185, pp. 210–226, 2017.

[69] I. Scheider, M. Pfuff, and W. Dietzel, "Simulation of hydrogen assisted stress corrosion cracking using the cohesive model," *Engineering Fracture Mechanics*, vol. 75, no. 15, pp. 4283–4291, 2008.

[70] L. Cupertino-Malheiros, T. K. Mandal, F. Thébault, and E. Martínez-Pañeda, "On the suitability of single-edge notch tension (SENT) testing for assessing hydrogen-assisted cracking susceptibility," *Engineering Failure Analysis*, vol. 162, p. 108360, 2024.

[71] S. Yuan, Y. Zhu, L. Zhao, S. Liang, M. Huang, and Z. Li, "Key role of plastic strain gradient in hydrogen transport in polycrystalline materials," *International Journal of Plasticity*, vol. 158, p. 103409, 2022.

[72] E. Martínez-Pañeda, S. Del Busto, C. F. Niordson, and C. Betegón, "Strain gradient plasticity modeling of hydrogen diffusion to the crack tip," *International Journal of Hydrogen Energy*, vol. 41, no. 24, pp. 10265–10274, 2016.

[73] P. K. Kristensen, C. F. Niordson, and E. Martínez-Pañeda, "A phase field model for elastic-gradient-plastic solids undergoing hydrogen embrittlement," *Journal of the Mechanics and Physics of Solids*, vol. 143, p. 104093, 2020.

[74] E. Martínez-Pañeda, C. F. Niordson, and R. P. Gangloff, "Strain gradient plasticity-based modeling of hydrogen environment assisted cracking," *Acta Materialia*, vol. 117, pp. 321–332, 2016.

[75] E. Ogosi, A. Siddiq, U. B. Asim, and M. E. Kartal, "Crystal plasticity based study to understand the interaction of hydrogen, defects and loading in austenitic stainless-steel single crystals," *International Journal of Hydrogen Energy*, vol. 45, no. 56, pp. 32632–32647, 2020.

[76] S. Yuan, Y. Zhu, M. Huang, S. Liang, and Z. Li, "Dislocation-density based crystal plasticity model with hydrogen-enhanced localized plasticity in polycrystalline face-centered cubic metals," *Mechanics of Materials*, vol. 148, p. 103472, 2020.

[77] V. Singh, A. Raj, Y. Charles, and D. K. Mahajan, "Hydrogen embrittlement in Nickel oligocrystals: Experimentation and crystal plasticity-phase field fracture modeling," *International Journal of Hydrogen Energy*, vol. 84, pp. 667–681, 2024.

[78] R. Kumar and D. K. Mahajan, "Hydrogen distribution in metallic polycrystals with deformation," *Journal of the Mechanics and Physics of Solids*, vol. 135, p. 103776, 2020.

[79] J. J. Rimoli and M. Ortiz, "A three-dimensional multiscale model of intergranular hydrogen-assisted cracking," *Philosophical Magazine*, vol. 90, no. 21, pp. 2939–2963, 2010.

[80] T. Zirkle, L. Costello, and D. L. McDowell, "Crystal Plasticity Modeling of Hydrogen and Hydrogen-Related Defects in Initial Yield and Plastic Flow of Single-Crystal Stainless Steel 316L," *Metallurgical and Materials Transactions A: Physical Metallurgy and Materials Science*, vol. 52, no. 9, pp. 3961–3977, 2021.

[81] A. Tondro, M. Taherijam, and H. Abdolvand, "Diffusion and redistribution of hydrogen atoms in the vicinity of localized deformation zones," *Mechanics of Materials*, vol. 177, no. December 2022, p. 104544, 2023.

[82] P. Sofronis, Y. Liang, and N. Aravas, "Hydrogen induced shear localization of the plastic flow in metals and alloys," *European Journal of Mechanics, A/-Solids*, vol. 20, no. 6, pp. 857–872, 2001.

[83] R. Depraetere, W. De Waele, and S. Hertelé, "Fully-coupled continuum damage model for simulation of plasticity dominated hydrogen embrittlement mechanisms," *Computational Materials Science*, vol. 200, p. 110857, 2021.

[84] L. Anand, Y. Mao, and B. Talamini, "On modeling fracture of ferritic steels due to hydrogen embrittlement," *Journal of the Mechanics and Physics of Solids*, vol. 122, pp. 280–314, 2019.

[85] D. F. Sarzosa, M. Paredes, and C. Ruggieri, "Fracture prediction on hydrogen-charge notched samples using a stress-state-dependent phenomenological model," *Engineering Fracture Mechanics*, vol. 303, p. 110145, 2024.

[86] H. Yu, J. S. Olsen, A. Alvaro, L. Qiao, J. He, and Z. Zhang, "Hydrogen informed Gurson model for hydrogen embrittlement simulation," *Engineering Fracture Mechanics*, vol. 217, p. 106542, 2019.

[87] A. Nagao, M. Dadfarnia, B. P. Somerday, P. Sofronis, and R. O. Ritchie, "Hydrogen-enhanced-plasticity mediated decohesion for hydrogen-induced intergranular and "quasi-cleavage" fracture of lath martensitic steels," *Journal of the Mechanics and Physics of Solids*, vol. 112, pp. 403–430, 2018.

[88] P. Novak, R. Yuan, B. P. Somerday, P. Sofronis, and R. O. Ritchie, "A statistical, physical-based, micro-mechanical model of hydrogen-induced intergranu-

lar fracture in steel," *Journal of the Mechanics and Physics of Solids*, vol. 58, no. 2, pp. 206–226, 2010.

[89] P. Kumar, M. M. Ludhwani, S. Das, V. Gavini, A. Kanjarla, and I. Adlakha, "Effect of hydrogen on plasticity of α-Fe: A multi-scale assessment," *International Journal of Plasticity*, vol. 165, no. December 2022, 2023.

[90] I. Benedetti, V. Gulizzi, and A. Milazzo, "Grain-boundary modelling of hydrogen assisted intergranular stress corrosion cracking," *Mechanics of Materials*, vol. 117, pp. 137–151, 2018.

[91] S. Jothi, T. N. Croft, and S. G. Brown, "Multiscale multiphysics model for hydrogen embrittlement in polycrystalline nickel," *Journal of Alloys and Compounds*, vol. 645, no. S1, pp. S500–S504, 2015.

[92] H. ul Hassan, K. Govind, and A. Hartmaier, "Micromechanical modelling of coupled crystal plasticity and hydrogen diffusion," *Philosophical Magazine*, vol. 99, no. 1, pp. 92–115, 2019.

[93] D. Depriester, J. Goulmy, and L. Barrallier, "Crystal plasticity simulations of in situ tensile tests: A two-step inverse method for identification of cp parameters, and assessment of cpfem capabilities," *International Journal of Plasticity*, vol. 168, p. 103695, 2023.

[94] C. Hardie, D. J. Long, E. Demir, E. Tarleton, and F. P. Dunne, "A robust and efficient hybrid solver for crystal plasticity," *International Journal of Plasticity*, vol. 170, p. 103773, 2023.

[95] Y. Huang, "A user-material subroutine incorporating single crystal plasticity in the abaqus finite element program," *Mech. Resport 178*, 1991.

[96] T. Yalcinkaya, W. A. M. Brekelmans, and M. G. D. Geers, "BCC single crystal plasticity modeling and its experimental identification," *Modelling and Simulation in Materials Science and Engineering*, vol. 16, no. 8, p. 085007, 2008.

[97] C.-S. Han, H. Gao, Y. Huang, and W. D. Nix, "Mechanism-based strain gradient crystal plasticity—i. theory," *Journal of the Mechanics and Physics of Solids*, vol. 53, no. 5, pp. 1188–1203, 2005.

[98] G. I. Taylor, "The mechanism of plastic deformation of crystals. part i.—theoretical," *Proceedings of the Royal Society of London. Series A, Containing Papers of a Mathematical and Physical Character*, vol. 145, no. 855, pp. 362–387, 1934.

[99] H. Mughrabi, "The α-factor in the taylor flow-stress law in monotonic, cyclic and quasi-stationary deformations: Dependence on slip mode, dislocation arrangement and density," *Current Opinion in Solid State and Materials Science*, vol. 20, no. 6, pp. 411–420, 2016.

[100] E. Günay, "Application of a lower order strain gradient crystal plasticity model on polycrystalline deformation and nanoscratching analyses," Master's thesis, Middle East Technical University, 2024.

[101] O. Bulut, E. Günay, T. O. Fenercioglu, and T. Yalçinkaya, "Analysis of additively manufactured anisotropic microstructures through crystal plasticity frameworks," *Materials Research Proceedings*, vol. 28, pp. 179–188, 2023.

[102] E. Günay, O. Bulut, and T. Yalçinkaya, "Examination of intrinsic and extrinsic size effect in thin specimens through crystal plasticity frameworks," *Materials Research Proceedings*, vol. 28, pp. 1471–1480, 2023.

[103] E. Günay, M. Özdemir, and T. Yalçinkaya, "Nanoscratching of polycrystalline copper examined through strain gradient crystal plasticity," *Procedia Structural Integrity*, vol. 61, pp. 34–41, 2024.

[104] K. Park, G. H. Paulino, and J. R. Roesler, "A unified potential-based cohesive model of mixed-mode fracture," *Journal of the Mechanics and Physics of Solids*, vol. 57, no. 6, pp. 891–908, 2009.

[105] K. Park and G. H. Paulino, "Computational implementation of the PPR potential-based cohesive model in ABAQUS: Educational perspective," *Engineering Fracture Mechanics*, vol. 93, pp. 239–262, 2012.

[106] A. Cerrone, P. Wawrzynek, A. Nonn, G. H. Paulino, and A. Ingraffea, "Implementation and verification of the Park-Paulino-Roesler cohesive zone model in 3D," *Engineering Fracture Mechanics*, vol. 120, pp. 26–42, 2014.

[107] C. V. Di Leo and L. Anand, "Hydrogen in metals: A coupled theory for species diffusion and large elastic–plastic deformations," *International Journal of Plasticity*, vol. 43, pp. 42–69, 2013.

[108] A. H. Krom, R. W. Koers, and A. Bakker, "Hydrogen transport near a blunting crack tip," *Journal of the Mechanics and Physics of Solids*, vol. 47, no. 4, pp. 971–992, 1999.

[109] E. D. Hondros and M. P. Seah, "Theory of Grain Boundary Segregation in Terms of Surface Adsorption Analogues," *Metallurgical Transactions A*, vol. 8 A, no. 9, pp. 1363–1371, 1977.

[110] D. E. Jiang and E. A. Carter, "First principles assessment of ideal fracture energies of materials with mobile impurities: implications for hydrogen embrittlement of metals," *Acta Materialia*, vol. 52, no. 16, pp. 4801–4807, 2004.

[111] S. Serebrinsky, E. A. Carter, and M. Ortiz, "A quantum-mechanically informed continuum model of hydrogen embrittlement," *Journal of the Mechanics and Physics of Solids*, vol. 52, no. 10, pp. 2403–2430, 2004.

[112] A. Alvaro, I. Thue Jensen, N. Kheradmand, O. M. Løvvik, and V. Olden, "Hydrogen embrittlement in nickel, visited by first principles modeling, cohesive zone simulation and nanomechanical testing," *International Journal of Hydrogen Energy*, vol. 40, no. 47, pp. 16892–16900, 2015.

[113] T. Yalçinkaya, G. Ö. Güngör, S. O. Çakmak, and C. Tekoğlu, "A Micromechanics Based Numerical Investigation of Dual Phase Steels," *Procedia Structural Integrity*, vol. 21, pp. 61–72, 2019.

[114] C. Tekoglu, "Representative volume element calculations under constant stress triaxiality, Lode parameter, and shear ratio," *International Journal of Solids and Structures*, vol. 51, no. 25-26, pp. 4544–4553, 2014.

[115] T. Yalçinkaya, B. Tatli, I. E. Ünsal, and I. U. Aydiner, "Crack Initiation and Propagation in Dual-phase Steels Through Crystal Plasticity and Cohesive Zone Frameworks," *Procedia Structural Integrity*, vol. 42, no. 2019, pp. 1651–1659, 2022.

[116] I. U. Aydiner, B. Tatli, and T. Yalçinkaya, “Micromechanical modeling of failure in dual phase steels,” in *Materials Research Proceedings*, vol. 28, pp. 1443–1452, 2023.

[117] I. U. Aydiner, B. Tatli, and T. Yalçinkaya, “Investigation of failure mechanisms in dual-phase steels through cohesive zone modeling and crystal plasticity frameworks,” *International Journal of Plasticity*, vol. 174, p. 103898, 2024.

[118] R. Quey, P. R. Dawson, and F. Barbe, “Large-scale 3D random polycrystals for the finite element method: Generation, meshing and remeshing,” *Computer Methods in Applied Mechanics and Engineering*, vol. 200, no. 17-20, pp. 1729–1745, 2011.